Extreme g-tensor anisotropy and its insensitivity to structural distortions in a family of linear two-coordinate Ni(I) bis-N-heterocyclic carbene complexes

William J. M. Blackaby[1], Katie L. M. Harriman[2], Samuel M. Greer[3,4], Andrea Folli[6], Stephen Hill[3,5], Vera Krewald[7], Mary F. Mahon[1], Damien M. Murphy[6], Muralee Murugesu[2], Emma Richards[6*], Elizaveta Suturina[1*] and Michael K. Whittlesey[1]

[1]Department of Chemistry, University of Bath, Claverton Down, Bath BA2 7AY, U. K.

[2]Department of Chemistry and Biomolecular Sciences, University of Ottawa, 10 Marie Curie, Ottawa, Ontario K1N 6N5, Canada

[3]National High Magnetic Field Laboratory, Florida State University, Tallahassee, FL 32310, United States

[4]Department of Chemistry, Florida State University, Tallahassee, FL 32306, United States.

[5]Department of Physics, Florida State University, Tallahassee, FL 32306, United States.

[6]School of Chemistry, Cardiff University, Park Place, Cardiff CF10 3AT, U. K.

[7]Theoretical Chemistry, TU Darmstadt, Alarich-Weiss-Strasse 4, 64287 Darmstadt, Germany

ABSTRACT: We report a new series of homoleptic Ni(I) bis-N-heterocyclic carbene complexes with a range of torsion angles between the two ligands from 68° to 90°. Electron paramagnetic resonance (EPR) measurements revealed a strongly anisotropic **g**-tensor in all complexes with a small variation in $g_{\parallel}$~ (5.6-5.9) and $g_{\perp}$~ 0.6. The energy of the first excited state identified by variable-field far-infrared magnetic spectroscopy (FIRMS) and SOC-CASSCF/NEVPT2 calculations is in the range 270 to 650 cm^{-1}. Magnetic relaxation measured by alternating current (AC) susceptibility up to 10 K is dominated by Raman and direct processes. *Ab initio* ligand field analysis reveals that a torsion angle smaller than 90° causes the splitting between doubly occupied d_{xz} and d_{yz} orbitals which has little effect on the magnetic properties, while the temperature dependence of the magnetic relaxation appears to have no correlation with the torsion angle.

INRODUCTION

Understanding magneto-structural correlations in transition metal complexes is one of the key aspects in the rational design of magnetic materials.[1] In particular, the connection between magnetic anisotropy and the structure of coordination compounds has attracted a lot of attention, as it is linked to slow relaxation of the magnetization.[2-6]

Anisotropy of the magnetic properties at very low temperature is characterized by the effective **g**-tensor of the ground magnetic sublevels. At increased temperature, other magnetic sublevels get populated, which affects the overall magnetic properties. The energy separation between magnetic sublevels at zero magnetic field is called zero-field splitting (ZFS) - another important characteristic of magnetic anisotropy. Both ZFS and **g**-tensor anisotropy result from spin-orbit coupling (SOC), which is most pronounced when the orbital momentum is unquenched and the SOC constant is large. An unquenched orbital momentum is retained by a high symmetry of the first coordination sphere that leaves orbitals with unpaired electron(s) degenerate. For this reason, linear two-coordinate transition metal complexes (MX_2) are particularly interesting.[2, 7-8]

There are several reported examples of transition metal MX_2 complexes exhibiting slow magnetic relaxation. Metal complexes with a $3d^7$ electronic configuration, such as those of cobalt(II)[9] and iron(I),[10-12] have the largest magnetic anisotropy and the slowest relaxation of the magnetization.

A cobalt(II) dialkyl complex reported by Bunting et al.[9] has the maximum possible contribution of the orbital momentum $|M_L|$=3 due to a non-Aufbau electronic configuration $(d_{xy}, d_{x^2-y^2})^3(d_{xz}, d_{yz})^3(d_{z^2})^1$. This leads to a doubly degenerate $^4\Phi$ ground state ($C_{\infty v}$ point group notation), which due to SOC, splits into four Kramers doublets (KD) with M_J=±9/2, ±7/2, ±5/2 and ±3/2. The ground KD with M_J=±9/2 has theoretical limit for the effective **g**-tensor of (0, 0, 12). A recently reported study of a cobalt(II) amido complex also shows a non-Aufbau ground state, however, π-antibonding interactions due to amido lone pair split (d_{xz}, d_{yz}) orbitals and quench orbital momentum reducing overall magnetic anisotropy.[13]

The electronic structure of an iron(I) dialkyl complex reported by Zadrozny et al.[10] differs from the cobalt(II) analogue since the low oxidation state allows for a more pronounced 3*d*-4*s* mixing which stabilizes the d_{z^2} orbital, leading to a

$(d_{z^2})^2(d_{xy}, d_{x^2-y^2})^3(d_{xz}, d_{yz})^2$ electronic configuration. This assignment was confirmed by multipole analysis of the X-Ray diffraction data.[14] This means that the orbital contribution is smaller $|M_L|$=2 and the ground state $^4\Delta$ splits into four KDs with M_J=$\pm$7/2, $\pm$5/2, $\pm 3/2$ and $\pm 1/2$. The theoretical limit of M_J=$\pm$7/2 effective **g**-tensor is (0, 0, 10). An iron(I) bis-amido complex reported by Werncke et al.[11] has a similar ordering of *d*-orbitals, however the anisotropy of metal-ligand π-antibonding interaction splits the (d_{xz}, d_{yz}) orbital pair.[15] This is also observed in another recently reported iron(I) bis-amido complex.[13] However, orbital splitting does not quench orbital momentum in those complexes. In contrast, an iron(I) bis-carbene complex reported by Samuel et al.[12] features anisotropy of the metal-ligand π interaction that lowers the effective anisotropy of the **g**-tensor.

Complexes with $3d^8$ configuration, in particular iron(II), were among the first MX_2 complexes reported to show slow magnetic relaxation and their electronic structure and magnetic anisotropy has been studied thoroughly.[16-19] It was shown by *ab initio* analysis that changes in the ligand environment has little effect on the $^5\Delta$ ground state as the orbital contribution $|M_L|$=2 remains largely unquenched in all cases.[20]

In the case of cobalt(I) bis-N-heterocyclic carbene (NHC) complexes, a strong correlation between the ZFS parameters and the interligand torsion angle has been reported.[21] In that study, only one of the three carbene ligands leads to an observation of the slow relaxation of the magnetization.

In this work, we focus on nickel(I) bis-NHC complexes i.e. a $3d^9$ configuration, where only one example has been published previously by some of us.[22] We now report a detailed analysis of static and dynamic magnetic properties and electronic structures of three new nickel(I) bis-NHC complexes with a wide range of interligand torsion angles.

METHODS

Synthesis and general procedures. All manipulations were carried out using standard Schlenk line, high vacuum and glovebox techniques. Solvents were purified using an MBraun SPS solvent system (hexane, pentane, diethyl ether, toluene, dichloromethane) or distilled from sodium benzophenone ketyl (benzene, THF), before sparging with argon and stored over regenerated molecular sieves. C_6D_6 and CD_2Cl_2 were vacuum transferred from K and CaH_2 respectively. NMR spectra were recorded at 298 K on Bruker Avance 400 and 500 MHz NMR spectrometers and referenced to solvent signals: benzene (^{1}H, δ 7.16; ^{13}C{^{1}H}, δ 128.1), dichloromethane (^{1}H, δ 5.32; ^{13}C{^{1}H}, δ 53.8). Elemental analyses were performed by Elemental Microanalysis Analytical Services, Okehampton, Devon, U. K.. $Ni(COD)_2$ (Strem) and $Ni(PPh_3)_2Br_2$ (Sigma) were used as received. **2-6Mes** was prepared as previously reported.[22]

Ni(6Xyl)(PPh$_3$)Br (1-6Xyl). 6Xyl (300 mg, 1.03 mmol),[23] $Ni(COD)_2$ (141 mg, 0.51 mmol) and $Ni(PPh_3)_2Br_2$ (381 mg, 0.51 mmol) were combined in THF and stirred for 1 h in a J. Young's ampule fitted with a PTFE tap. The resulting yellow solution was reduced to dryness, washed with Et_2O (2 x 10 mL) and recrystallized from THF/hexane. Yield: 530 mg (71%). ^{1}H NMR (C_6D_6, 500 MHz): δ 29.4 (br s), 16.4 (br s), 10.8 (s), 9.8 (br s), 8.5 (br s), 8.1 (br s), 2.2 (br s), 1.9 (br s), 0.7 (br s), -1.1 (br s), -17.1 (v br s). Anal. calcd. (found) for $C_{38}H_{39}N_2PNiBr$ (%): C 65.83 (65.50), H 5.67 (5.50), N 4.04 (4.05). Solution magnetic moment (Evans method): 2.0 μB in benzene at 298 K. Molecular structure is shown on Figure S1.

Ni(7Mes)(PPh$_3$)Br (1-7Mes). As for **1-6Xyl**, but using 7Mes (100 mg, 0.30 mmol),[23] $Ni(COD)_2$ (41 mg, 0.15 mmol) and $Ni(PPh_3)_2Br_2$ (111 mg, 0.15 mmol). Yield: 148 mg (67%). ^{1}H NMR (C_6D_6, 500 MHz): δ 12.3 (br s), 10.6 (br s), 9.9 (br s), 8.6 (br s), 8.1 (br s), 4.5 (s), 3.3 (br s), 2.9 (m), 2.8 (s), 2.5 (s), 2.4 (br s), 1.8 (v br s), 0.9 (br s), -1.3 (br s). Anal. calcd. (found) for $C_{41}H_{45}N_2PNiBr$ (%): C 66.96 (67.22), H 6.17 (6.26), N 3.81 (3.41). Solution magnetic moment (Evans method): 1.8 μB in benzene at 298 K.

Ni(7Xyl)(PPh$_3$)Br (1-7Xyl). As for **1-6Xyl**, but using 7Xyl (250 mg, 0.82 mmol),[23] $Ni(COD)_2$ (112 mg, 0.41 mmol) and $Ni(PPh_3)_2Br_2$ (303 mg, 0.41 mmol). Analytically pure product was achieved by recrystallization from C_6H_6/hexane. Yield: 377 mg (65 %). ^{1}H NMR (C_6D_6, 500 MHz): δ 11.7 (br s), 10.6 (br s), 10.1 (br s), 8.5 (br s), 7.9 (br s), 3.4 (br s), 2.8 (s), 2.4-2.3 (br m), 0.9 (br s), -1.2 (br s). Anal. calcd. (found) for $C_{39}H_{41}N_2PNiBr \cdot 0.5C_6H_6$ (%): C 67.59 (67.80), H 5.94 (5.76), N 3.75 (3.61). Solution magnetic moment (Evans method): 1.9 μB in benzene at 298 K. Molecular structure is shown on Figure S1.

[Ni(6Xyl)$_2$]$_2$Br (2-6Xyl). A flame dried Schlenk flask was charged with **1-6Xyl** (96 mg, 0.14 mmol) and 6Xyl (64 mg, 0.22 mmol) in THF (30 mL) and the mixture stirred for 16 h to form an off-white suspension. The precipitate was isolated by cannula filtration, washed with Et_2O (2 x 10 mL) and dried under reduced pressure. Recrystallization from CH_2Cl_2/hexane yielded an off-white product. Yield: 54 mg (54%). ^{1}H NMR (CD_2Cl_2, 500 MHz): δ 54.3 (br s, 4H), 52.1 (br s, 8H), -13.3 (br s, 24H), -15.6 (s, 4H), -21.2 (s, 8H). Anal. calcd. (found) for $C_{40}H_{48}N_4NiBr$ (%): C 66.41 (66.62), H 6.69 (6.70), N 7.74 (7.54). Solution magnetic moment (Evans method): 3.3 μB in dichloromethane at 298 K.

[Ni(7Mes)$_2$]$_2$Br (2-7Mes). As for **2-6Xyl**, but using **1-7Mes** (200 mg, 0.34 mmol) and 7Mes (171 mg, 0.51 mmol). Yield: 181 mg (66%). ^{1}H NMR (CD_2Cl_2, 500 MHz, 298 K): δ 49.2 (br s, 8H), 38.7 (br s, 8H), -8.3 (s, 12H), -11.2 (br s, 24H), -17.7 (s, 8H). Despite multiple recrystallizations, efforts to determine accurate elemental analyses repeatedly gave a low %C value e.g. Anal. calcd. (found) for $C_{46}H_{60}N_4NiBr$ (%): C 68.41 (67.43), H 7.49 (7.51), N 6.93 (6.82). Solution magnetic moment (Evans method): 3.0 μB in dichloromethane at 298 K.

[Ni(7Xyl)$_2$]$_2$Br (2-7Xyl). As for **2-6Xyl**, but using **1-7Mes** (200 mg, 0.35 mmol) and 7Xyl (162 mg, 0.53 mmol). Yield 205 mg (77 %). ^{1}H NMR (CD_2Cl_2, 500 MHz): δ 51.1 (br s, 8H), 40.0 (br s, 8H), -11.8 (br s, 24H), -14.1 (s, 4H), -18.2 (s, 8H). Anal. calcd. (found) for $C_{42}H_{52}N_4NiBr$ (%): C 67.13 (67.39), H 6.97 (6.82), N 7.46 (7.31). Solution magnetic moment (Evans method): 3.1 μB in dichloromethane at 298 K.

SQUID magnetometry. Magnetic susceptibility measurements were obtained using a Quantum Design SQUID magnetometer MPMS-XL7 operating between 1.8 and 300 K. Direct current (dc) measurements were performed on polycrystalline samples of 26 mg, 27 mg, and 26 mg for **2-6Xyl**, **2-7Mes**, and **2-7Xyl** respectively. The samples were prepared under an inert atmosphere in an MBraun glovebox and wrapped in a polyethylene membrane. The samples were subjected to dc fields up to 7 T, and a 3.78 Oe driving field was used for alternating current (ac) measurements. The magnetization data was collected at 100 K to check for ferromagnetic impurities which were absent in all samples. Diamagnetic corrections were applied for the sample holder.

Electron paramagnetic resonance (EPR). Samples for EPR measurements were prepared under an N_2 atmosphere in a glovebox. A solution of each complex was prepared by dissolving ca. 4 mg of **2-6Xyl**/**7Mes**/**6Mes**/**7Xyl** in 100 μL of dry CH_2Cl_2. The solutions were transferred to an EPR tube, sealed in the glove box and then cooled to 77 K before rapid transfer to the pre-cooled EPR cavity. The X-band CW EPR measurements were performed on a Bruker EMX spectrometer utilizing an ER 072 magnet/ ER 081 power supply combination (maximum field 0.6 T), an ER4119HS resonator, operating at 100 kHz field modulation and 10 mW microwave power at 140 K. Additional EPR measurements were performed on a Bruker E500 spectrometer equipped with an Oxford Instruments liquid-helium cryostat utilizing an ER 073 magnet/ ER 083 power supply combination (maximum field 1.45 T), an ER4102ST resonator, operating at 100 kHz field modulation and 0.63 mW microwave power at 10 K.

High Frequency Electron Paramagnetic Resonance spectra were collected on microcrystalline powder samples contained in a polyethylene cup. The transmission-type spectrometer used in this study employed a 17 T superconducting magnet.[24] Microwave frequencies were generated in the 52 to 314 GHz range using a phase-locked Virginia Diodes source combined with a series of frequency multipliers. The field modulated signal was detected by an InSb hot-electron bolometer (QMC Ltd., Cardiff, U.K.). Temperature control was realized using an Oxford Instruments (Oxford, U.K.) continuous-flow cryostat. Angle dependent spectra of single crystals of **2-NHC** were recorded at 16.77 GHz using a high-sensitivity cavity perturbation technique. For this measurement the microwaves were generated and detected by a millimeter-wave vector network analyzer, MVNA, the details of which have been described elsewhere.[25-26] The magnetic field and cryostat assembly are those associated with a Quantum Design Physical Property Measurement System, PPMS. One alteration from the typical PPMS design was that the 7 T superconducting magnet is orientated horizontal relative to the sample chamber. This split solenoid, vertical-bore magnet thus facilitates in-situ rotation of the cavity relative to the applied field. Once the field was aligned parallel to the hard-plane, spectra were recorded at multiple frequencies for a reliable determination of the effective *g*-value.

Far-infrared magnetic spectroscopy (FIRMS). Far-IR spectra were recorded using a Bruker Vertex 80v vacuum FTIR spectrometer with a resolution of 0.12 cm^{-1} at 4.2 K, over a range of 7 - 1000 cm^{-1}. The transmitted IR radiation was detected using a composite Si bolometer placed directly beneath the sample. The sample was mounted such that the applied field was parallel to the direction of light propagation (Faraday geometry).[27] Four spectra were recorded at each field between 0 - 17 T in 1 T increments. To differentiate the magnetic from non-magnetic transitions, each spectrum was divided by a reference spectrum. This procedure was done for multiple choices of reference, all of which furnish final spectra with consistent field dependent behavior. The divided spectra in the text were prepared by using the spectrum recorded at 4 T higher applied field as the reference.

***Ab initio* calculations.** Starting from the X-ray crystal structures, geometry optimizations were carried out with ORCA[28-29] by either relaxing only the H-atom positions or the full molecule. The density functional chosen was BP86 together with dispersion corrections with Becke-Johnson damping and zeroth order relativistic corrections including the one-center approximation. The scalar-relativistically recontracted ZORA-def2-TZVP basis set was used on all atoms except C and H, where ZORA-def2-SVP was used.[30-31] To speed up the calculations, the resolution of the identity (RI) approximation was invoked together with the SARC/J auxiliary basis. The grid and integration accuracy were both increased to 7 in ORCA nomenclature. Tight SCF and geometry convergence criteria were used.

CASSCF and strongly contracted NEVPT2 calculations including spin-orbit coupling were performed using a def2-TZVP basis set on all atoms and def2-TZVP/C auxiliary basis sets due to the use of the RI approximation. The active space was defined as nine electrons in five orbitals. Five roots with multiplicity two were calculated. Based on this wavefunction, the **g**-tensor, susceptibility and magnetisation were calculated. *Ab initio* ligand field analysis was employed to extract energies and composition of the *d*-orbitals.[32]

RESULTS AND DISCUSSION

The synthesis of the new complexes **2-6Xyl**, **2-7Mes** and **2-7Xyl** (Scheme 1) involved reactions of the three-coordinate Ni(I) precursors Ni(NHC)(PPh_3)Br (**1-NHC**) (Figure S1) with an excess of the corresponding free NHC in THF solution at room temperature. The two-coordinate products were isolated as off-white or pale-yellow solids in yields of 54-77 %.

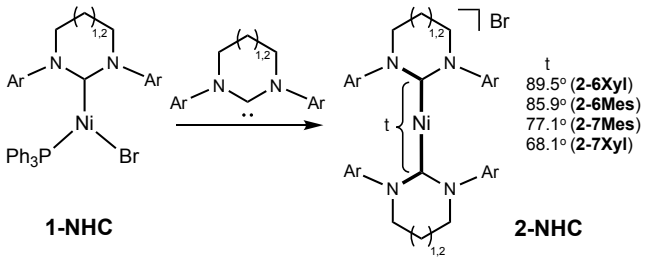

Scheme 1. Synthesis of two-coordinate [Ni(NHC)$_2$]Br complexes **2-6Mes**: n = 1, Ar = 2,4,6-$Me_3C_6H_2$; **2-6Xyl**: n = 1, Ar = 2,6-$Me_2C_6H_3$; **2-7Mes**: n = 2, Ar = 2,4,6-$Me_3C_6H_2$; **2-7Xyl**: n = 2, Ar = 2,6-$Me_2C_6H_3$ with a pronounced variation of the interligand torsion angle (τ).

Isolation of crystals suitable for X-ray crystallography revealed linear C_{NHC}-Ni-C_{NHC} (178.92(11)–179.78(15)°) arrangements in **2-NHC** and very little variation in Ni-C bond lengths (1.943(2)-1.959(3) Å, Figure 1). The crystal packing varies with the type of NHC: **2-6Xyl** - *C*2/c, **2-7Mes** - *P*ca2$_1$, **2-6Mes** - *P*2$_1$, **2-7Xyl** – *C*2/c. The shortest intermolecular Ni···Ni distances are 10.4, 10.6, 10.3, and 10.4 Å, respectively (Figure S2). The asymmetric units of **2-6Xyl** and **2-7Xyl** each contain half of a cation; the remainder being generated by virtue of a 2-fold crystallographic rotation axis in each case. There is solvent of crystallization present, in a CH_2Cl_2:cation ratio of 2:1 for **2-6Xyl** and **2-7Xyl**, while the comparative ratio for **2-7Mes** is 1:1. The crystal structures also highlight variation in the torsion angle between the two NHCs coordinated to each nickel center. In particular, the angles between mean planes based on the metal center, ligand nitrogens and carbene-carbon for each ligand decrease from 89.49(11)° for **2-6Xyl** to 85.82(13)° for **2-6Mes**, 77.85(11)° for **2-7Mes** and, smallest of all, 68.08(10)°, for **2-7Xyl**.

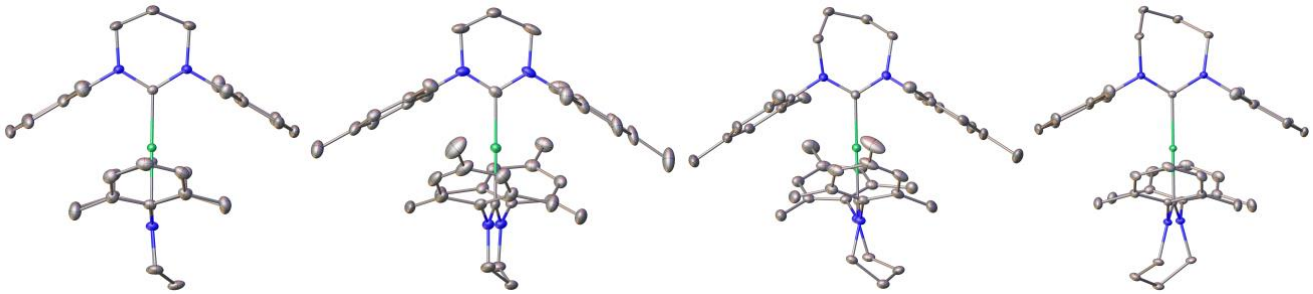

Figure 1. X-ray crystal structures of the cations in **2-6Xyl**, **2-6Mes, 2-7Mes** and **2-7Xyl** are shown from left to right. Color code: Ni -green, N-blue, C-grey. The minor disordered component of **2-6Mes** and hydrogen atoms have been omitted for clarity. Thermal ellipsoids are shown at 30% probability. The orientation is chosen so that one of the NHC planes is within the plane of the figure, highlighting the differences in the torsion angle between the two ligands.

Solution magnetic moment measurements of **2-NHC** in dichloromethane (Evans method) revealed μ_{eff} values of 3.0-3.3 μ_B, which is much higher than the spin-only value of 1.73 μ_B.

SQUID measurements of the magnetic susceptibility for polycrystalline powders under a 0.1 T static field also showed χT values at 300 K in the range of 1.2-1.3 cm^3 K mol^{-1} (3.1-3.2 μ_B) – much higher than the theoretical spin-only value of 0.375 cm^3 K mol^{-1}. Upon lowering the temperature, the χT value stayed nearly constant until approximately 5 K, where it decreased sharply suggesting a relatively small intermolecular interaction (Figure S11). The molar magnetization measured between 1.8 – 7 K and 0 – 7 T has near-saturation values of 1.7-1.9 μ_B (Figure S11). Assuming axial anisotropy of the **g**-tensor, the high temperature powder magnetic susceptibility and magnetization saturation values can be approximated as

$$\chi T = \frac{N\mu_B^2 S(S+1)}{9k}\left[g_\parallel^2 + 2g_\perp^2\right] \quad (1)$$

$$M_S = N\mu_B S\sqrt{\frac{g_\parallel^2 + 2g_\perp^2}{3}} \quad (2)$$

where N is Avogadro's number, S is the total spin, k is the Boltzmann constant and $g_\parallel, g_\perp$ are components of the **g**-tensor.

SQUID measurements are not sufficient to identify both $g_\parallel$ and $g_\perp$ independently, nevertheless, they set limitations on the combinations of $g_\parallel$ and $g_\perp$ (Figure S12).

Solution ^{1}H NMR spectra of **2-NHC** featured five strongly paramagnetically shifted peaks in the range -25 to 55 ppm at 298 K (Figures S6-S9). DFT calculations of the hyperfine tensors suggest that the proton paramagnetic shifts are dominated by a pseudo-contact contribution (PCS). Assuming uniaxial anisotropy, the best-fit for the axiality of the magnetic susceptibility tensor, $\Delta\chi_{ax}$, extracted from the PCS data at 298 K is 0.13-0.15 Å^3 (Table S2), suggesting a large anisotropy of the **g**-tensor with $g_\parallel^2 - g_\perp^2$ in the range of 19-22. Considering both paramagnetic NMR and SQUID constraints together, we can estimate $g_\parallel$~5 and $g_\perp$~2.

To determine definitively the *g*-values, we employed a series of high-field EPR experiments on a single crystal, as well as a polycrystalline powder of **2-6Mes** (Figure S16). These experiments revealed a remarkably anisotropic **g**-tensor: $g_\parallel$ = 5.42, $g_\perp$ = 0.36. This observation showed that an analogous measurement at X-band (9.5 GHz) would require a magnetic field above the maximum attainable for most X-band magnets (typically <1 T). The X-band results were therefore acquired using two magnet systems (see ESI). Measurements on frozen solutions of **2-NHC** showed that the $g_\parallel$ values for all complexes are in the range of 5.7-5.9 (Figure 2 and Figure S14) and $g_\perp$~ 0.6 (Figure 2); the differences between the solid-state and solution are likely due to small variations in the molecular structures. Such highly anisotropic **g**-tensors are uncommon for $3d^9$ electronic configuration. Examples of similar magnetic anisotropy in complexes with S=1/2 occur in actinide and lanthanide systems,[24] and some rare cases of low-spin d^5 complexes such as Os(III).[33-34]

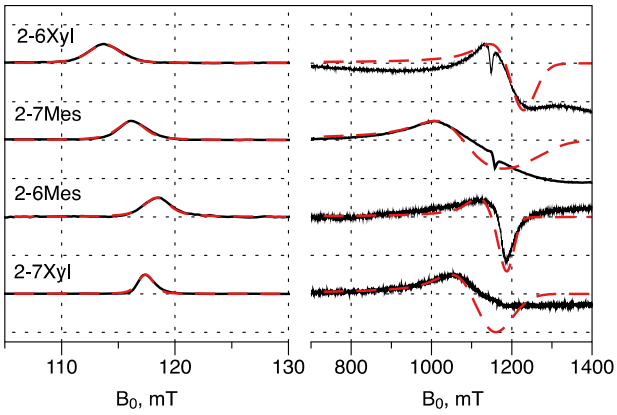

Figure 2. Continuous wave X-band EPR spectra of frozen CH_2Cl_2 solutions of **2-NHC** measured at 10 K up to 130 mT (Bruker EMX, 8" magnet) and from 700 to 1400 mT (Bruker E500, 10" magnet). The microwave frequencies from top to bottom are 9.3820, 9.3814, 9.3926 and 9.3928 GHz plotted normalized to 9.5 GHz. The red lines show EasySpin simulations with parameters given in Table 1.

Table 1. Experimental and *ab initio* calculated (shown in parentheses, CASSCF(9,5)/NEVPT2/def2-TZVP) **g**-tensors of **2-NHC**.

	g_1	g_2	g_3
2-6Xyl	0.55 (0.53)	0.56 (0.53)	5.887 (5.89)
2-7Mes	0.55 (0.60)	0.62 (0.66)	5.755 (5.77)
2-6Mes	0.565 (0.72)	0.585 (0.74)	5.66 (5.77)
2-7Xyl	0.58 (0.64)	0.602 (0.66)	5.70 (5.81)

The origin of the large magnetic anisotropy in **2-NHC** was unveiled by *ab initio* ligand field analysis (AI LFT) based on CASSCF(9,5)/NEVPT2 calculations (Figure 3).

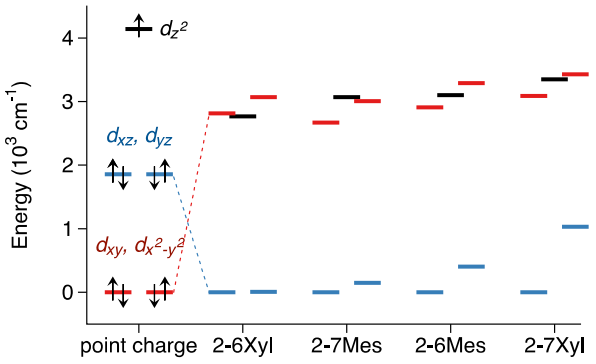

Figure 3. Ligand field splitting of *d*-orbitals expected for a linear two-coordinate system with point charges in comparison with the ligand field splitting in **2-NHC** calculated using AI LFT based on CASSCF(9,5)/NEVPT2/def2-TZVP (see also Figure S18 for AI LFT orbitals).

Following a simple crystal-field model, one would expect that the energetic ordering of the *d*-orbitals in a linear two-coordinate complex would be $(d_{xy}, d_{x^2-y^2}) < (d_{xz}, d_{yz}) < d_{z^2}$.[35] Hence, a d^9 configuration should yield an orbitally non-degenerate ground state $^2\Sigma^-$ with an almost isotropic **g**-tensor. Indeed, this is what is observed in the formally isoelectronic Cu(II) bis-amido complexes.[36] However, the AI LFT (Figure 3) suggests that the order of *d*-orbitals in **2-NHC** is completely different: $(d_{xz}, d_{yz}) < d_{z^2} \approx (d_{xy}, d_{x^2-y^2})$. The (d_{xz}, d_{yz}) orbital pair is stabilized due to strong π-back bonding from the NHC ligands, while d_{z^2} is stabilized by 3*d*-4*s* mixing. Both effects make the $(d_{xy}, d_{x^2-y^2})$ orbital pair that carries the largest orbital momentum projection $|M_L|$=2 highest in energy creating an orbitally degenerate ground state $^2\Delta$ with a very large **g**-tensor anisotropy (Table 1). The theoretical maximum for **g**-tensor anisotropy according to ligand field theory is (0,0,6), which is almost achieved in **2-NHC**.

Variation of the torsion angle between ligands across the series primarily affects the splitting of the (d_{xz}, d_{yz}) orbitals. They are degenerate in the case of ∠N-C-C-N = 90° (**2-6Xyl**), and their splitting increases as the torsion angle decreases (Figure 3). However, both orbitals (d_{xz}, d_{yz}) are doubly occupied and their energy splitting does not significantly affect the magnetic properties. The splitting of $(d_{xy}, d_{x^2-y^2})$ and relative position of d_{z^2} is much more important for the **g**-tensor anisotropy of **2-NHC**.

Such variation of the torsion angle in linear two-coordinate metal(I) bis-carbene complexes is expected to affect the magnetic properties of a $3d^6$ configuration (e.g. Mn(I)) where an odd number of electrons occupy the (d_{xz}, d_{yz}) orbitals, but the only examples of such complexes for manganese are [Mn(cAAC)$_2$], which feature Mn(II) and radical ligands.[37] Linear Fe(I) bis-carbene complexes may also be affected by ligand rotation if the highest energy (d_{xz}, d_{yz}) orbitals become degenerate with $(d_{xy}, d_{x^2-y^2})$ at a torsion angle of 0º, which seems to be the case for [Fe(cAAC)]$^+$, as it was reported to have large effective magnetic moment μ_{eff} ~5 μ_B (spin-only value is 3.8 μ_B) and slow magnetic relaxation.[12]

The separation between the ground doublet, and the first excited doublet in **2-6Mes** was measured by variable-field FIRMS spectroscopy to be ~643 cm^{-1} (Figures 4 and S17). *Ab initio* results for the SOC corrected first excited doublet state show some variation within the series: 653 cm^{-1} for **2-6Xyl**, 277 cm^{-1} for **2-7Mes,** 514 cm^{-1} for **2-6Mes** and 407 cm^{-1} for **2-7Xyl**. There appears to be no correlation between relative orientation of the two carbene ligands and predicted energy gap as more subtle non-bonding interactions with the N-aryl substituents of the ligands are responsible for splitting and mixing of $d_{x^2-y^2}, d_{xy}$ and d_{z^2} orbitals. A simple ligand field model suggests that the effects of SOC on a degenerate d_{xy} and $d_{x^2-y^2}$ orbital pair will produce two Kramers doublets M_J=±5/2 and =±3/2 separated by 2ζ where ζ is the spin-orbit coupling constant (Ni(I) $\zeta \approx 600$ cm^{-1}). This suggests that the first spin-orbit state exists ≥ 1200 cm^{-1} above the ground state, a prediction that is incompatible with the experimentally observed gap of ~643 cm^{-1} and suggests that an additional state is present. Examination of the AI LFT orbital splitting shows that the d_{z^2} orbital is similar in energy to the d_{xy} and $d_{x^2-y^2}$ orbitals and, thus, gives rise to a third low-lying Kramers doublet (Table S3). The *ab initio* calculations reveal that these orbitals are highly mixed, which makes qualitative rationalization of trends in excited state energies difficult. However, a simple ligand-field model (See SI) considering only the effects of SOC on a degenerate d_{z^2}, d_{xy} and $d_{x^2-y^2}$ orbital set results in three Kramers doublets, each separated by ζ (~600 cm^{-1}). This value is extremely close to the gap observed by the FIRMS experiments.

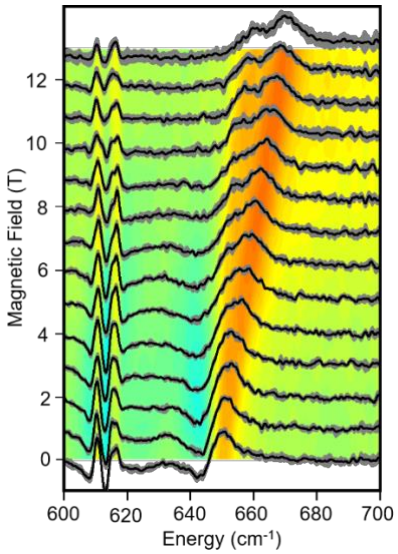

Figure 4. FIRMS spectra of **2-6Mes** divided by reference spectra recorded at 4 T larger field. The data have been offset by the magnetic field of each recorded spectrum. The grey shading around each spectrum is the standard deviation of the 4 recorded spectra at each field. The bottom surface is a 2D false color plot showing the evolution of the spectral features with applied field. The pair of features centered at ~612 cm^{-1} are field independent while the feature originating at ~643 cm^{-1} displays pronounced field dependence.

Such extraordinary magnetic anisotropy of $3d^9$ systems is the reason behind the previously observed slow relaxation of the magnetization in **2-6Mes**.[22] Even slower magnetic relaxation is

recorded for **2-6Xyl** and **2-7Mes**, while **2-7Xyl** shows a marginally faster relaxation rate (Figures 5-6 and S13).

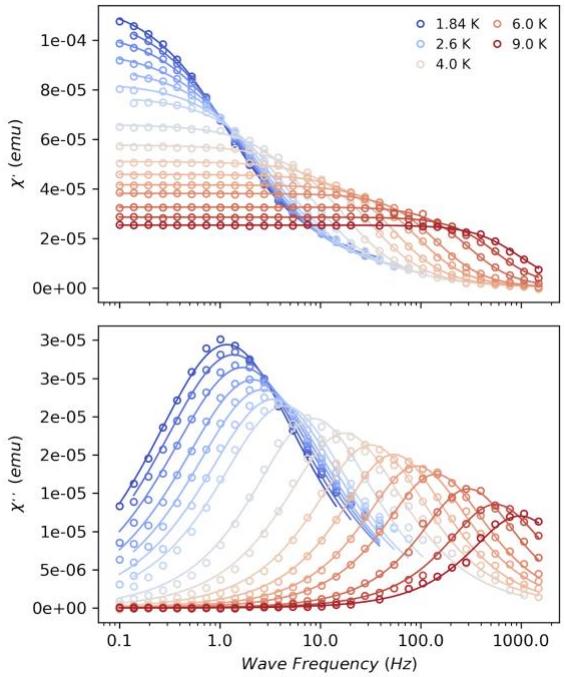

Figure 5. In-phase (χ'; top) and out-of-phase (χ"; bottom) powder magnetic susceptibility under 600 Oe applied magnetic field of **2-6Xyl** (circles) and generalized Debye model fits (lines) obtained with CC-FIT2.[38]

The fit of the temperature dependence of the relaxation data was done assuming Raman and direct processes (eq. (3))

$$\frac{1}{\tau} = CT^n + AT \qquad (3)$$

where A is the parameter for the direct process and C for the Raman process. Inclusion of the Orbach relaxation mechanism, which relies on a presence of a thermally accessible excited state, does not lead to an improvement of the fit in the measured low-T range (<10 K). It is expected for **2-NHC**, where the first excited state is well above 200 cm^{-1} according to FIRMS and *ab initio* results.

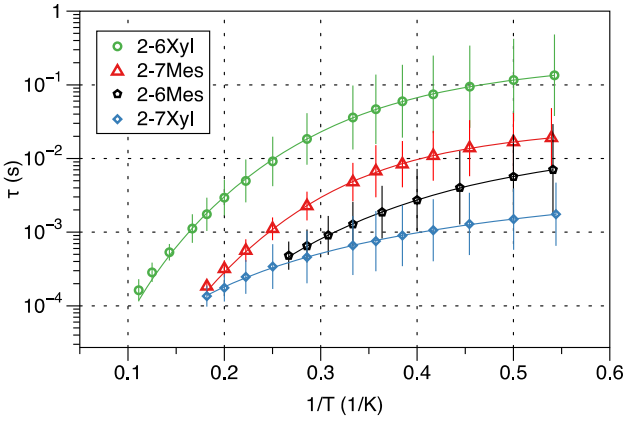

Figure 6. Temperature dependence of the relaxation times obtained under a 600 Oe applied DC field extracted from AC susceptibility measurements (symbols) and fit curves (solid lines) with Raman and direct processes (see text for details).

The best-fit parameters are listed in Table 2. The constants A and C of the respective direct and Raman processes increase from **2-6Xyl** to **2-7Xyl**. Meanwhile, the power in the Raman process, n, is smaller for **2-7Xyl** than for the rest of the series.

Table 2. Best-fit parameters of the temperature dependence of the relaxation time.

	C, s^{-1}K^{-n}	n	A, s^{-1}K^{-1}
2-6Xyl	0.04	5.6	3
2-7Mes	0.12	6.4	25
2-6Mes	2.1	5.2	50
2-7Xyl	28	3.2	206

Despite large uncertainties in the relaxation time, there is a noticeable difference at the low-temperature limit reflected in the large variation of best-fit parameters for both direct and Raman processes (Table 2). Relaxation data was acquired without any magnetic dilution, hence variations in dipolar couplings could be one of the reasons behind the low temperature differences. However, **2-6Xyl** and **2-7Xyl** have very similar crystal packing and **g**-tensors, hence, dipolar coupling is expected to be essentially the same for these two compounds. Nevertheless, the low-temperature relaxation time differs the most between **2-6Xyl** and **2-7Xyl**. Available *ab initio* studies of the magnetic relaxation in transition metal complexes[39-42] point out the importance of the molecular rigidity that can control the admixture of intramolecular vibrational modes that modulate the spin-Hamiltonian parameters via acoustic phonons, thus driving low temperature relaxation. The more rigid structure of the smaller carbene in **2-6Xyl** might therefore also contribute to its slower relaxation compared to the larger, less rigid NHC in **2-7Xyl**. Moreover, the difference in electrostatic polarisation of the donor atom may also affect Raman relaxation, as highlighted in the recent work by Lunghi et al.[43] Further studies of our Ni systems are needed to rationalize fully the magnetic relaxation behaviour of these compounds. Given the very similar electronic structures, **g**-tensor anisotropy and crystal packing, but different carbene-Ni-carbene torsion angles, **2-6Xyl** and **2-7Xyl** are excellent candidates for further *ab initio* analysis of the role of phonons in the low-temperaturelimit of Raman relaxation.

CONCLUSIONS

In summary, we have reported the synthesis and characterization of three new linear two-coordinate Ni(I) bis-NHC complexes with highly anisotropic **g**-tensor. We have characterized these compounds via a combination of advanced EPR spectroscopy, magnetometry and paramagnetic NMR analysis. *Ab initio* studies show that **2-NHC** has an orbitally degenerate ground state $^2\Delta$ due to carbene π-back bonding and 3*d*-4*s* mixing that completely changes the *d*-orbital splitting from that in a simple crystal field picture to $(d_{xz}, d_{yz}) < d_{z^2} \approx (d_{xy}, d_{x^2-y^2})$. This leads to a very large magnetic anisotropy $g_{\parallel}$~ (5.6-5.9) and $g_{\perp}$~ 0.6 as confirmed by EPR.

Contrary to expectations, the ligand rotation in the series was found to have little effect on the static magnetic properties as it mostly affects the splitting of the doubly occupied orbitals (d_{xz}, d_{yz}). There is a noticeable variation in the low temperature magnetic relaxation profile within the series **2-6Xyl**, **2-7Mes**, **2-6Mes** and **2-7Xyl**, however there is no correlation with the torsion angle. The electronic structure and crystal packing of **2-6Xyl** and **2-7Xyl** is very similar, hence an order of magnitude difference in the low-T magnetic relaxation time could be

attributed to differences in vibrational modes and spin-phonon coupling.

AUTHOR INFORMATION

Corresponding Authors

Emma Richards - School of Chemistry, Cardiff University, Park Place, Cardiff CF10 3AT, U.K.
Email: RichardsE10@cardiff.ac.uk
https://orcid.org/0000-0001-6691-2377

Elizaveta Suturina - Department of Chemistry, University of Bath, Claverton Down, Bath BA2 7AY, U.K.
Email: e.suturina@bath.ac.uk
https://orcid.org/0000-0003-4407-1882

Author Contributions

The manuscript was written through contributions of all authors. All authors have given approval to the final version of the manuscript.

ACKNOWLEDGMENTS

Work performed at the US National High Magnetic Field Laboratory is supported by the NSF (DMR-1644779) and the State of Florida. Additional support from the NSF (DMR-2004732 to S. H.) is also gratefully acknowledged. S. M. G acknowledges support from the National Science Foundation (NSF) Graduate Research Fellowship Program (DGE-1449440). Work performed at the University of Ottawa is graciously supported by the University of Ottawa, the Natural Sciences and Engineering Research Council of Canada, and the Canadian Foundation for Innovation. EAS and MKW thank the University of Bath for HPC facilities for computational time and for a PhD studentship (WJMB) respectively.

SUPPORTING INFORMATION

The Supporting Information is available free of charge at https://pubs.acs.org/doi/

Supporting information includes the details for X-Ray diffraction data, NMR spectra, SQUID magnetometry results, EPR and FIRMS spectra, and AI LFT molecular orbitals.

REFERENCES

1. Coronado, E., Molecular magnetism: from chemical design to spin control in molecules, materials and devices. *Nat. Rev. Mater.* **2020,** *5* (2), 87-104.
2. Bar, A. K.; Pichon, C.; Sutter, J.-P., Magnetic anisotropy in two- to eight-coordinated transition-metal complexes: Recent developments in molecular magnetism. *Coord. Chem. Rev.* **2016,** *308*, 346-380.
3. Meng, Y.-S.; Jiang, S.-D.; Wang, B.-W.; Gao, S., Understanding the Magnetic Anisotropy toward Single-Ion Magnets. *Acc. Chem. Res.* **2016,** *49* (11), 2381-2389.
4. Atanasov, M.; Aravena, D.; Suturina, E.; Bill, E.; Maganas, D.; Neese, F., First principles approach to the electronic structure, magnetic anisotropy and spin relaxation in mononuclear 3d-transition metal single molecule magnets. *Coord. Chem. Rev.* **2015,** *289-290*, 177-214.
5. Legendre, C. M.; Damgaard-Møller, E.; Overgaard, J.; Stalke, D., The Quest for Optimal 3 d Orbital Splitting in Tetrahedral Cobalt Single-Molecule Magnets Featuring Colossal Anisotropy and Hysteresis. *Eur. J. Inorg. Chem.* **2021,** *2021* (30), 3108-3114.
6. Bone, A. N.; Widener, C. N.; Moseley, D. H.; Liu, Z.; Lu, Z.; Cheng, Y.; Daemen, L. L.; Ozerov, M.; Telser, J.; Thirunavukkuarasu, K.; Smirnov, D.; Greer, S. M.; Hill, S.; Krzystek, J.; Holldack, K.; Aliabadi, A.; Schnegg, A.; Dunbar, K. R.; Xue, Z.-L., Applying Unconventional Spectroscopies to the Single-Molecule Magnets, Co(PPh3)2X2 (X=Cl, Br, I): Unveiling Magnetic Transitions and Spin-Phonon Coupling. *Chem. Eur. J.* **2021,** *27* (43), 11110-11125.
7. Layfield, R. A., Organometallic single-molecule magnets. *Organometallics* **2014,** *33* (5), 1084-1099.
8. Feng, M.; Tong, M.-L., Single ion magnets from 3d to 5f: developments and strategies. *Chem. Eur. J.* **2018,** *24* (30), 7574-+.
9. Bunting, P. C.; Atanasov, M.; Damgaard-Moller, E.; Perfetti, M.; Crassee, I.; Orlita, M.; Overgaard, J.; van Slageren, J.; Neese, F.; Long, J. R., A linear cobalt(II) complex with maximal orbital angular momentum from a non-Aufbau ground state. *Science* **2018,** *362* (6421), 1378.
10. Zadrozny, J. M.; Xiao, D. J.; Atanasov, M.; Long, G. J.; Grandjean, F.; Neese, F.; Long, J. R., Magnetic blocking in a linear iron(I) complex. *Nature Chem.* **2013,** *5*, 577-581.
11. Werncke, C. G.; Bunting, P. C.; Duhayon, C.; Long, J. R.; Bontemps, S.; Sabo-Etienne, S., Two-coordinate iron(I) complex Fe{N(SiMe3)(2)}(2) (-) : synthesis, properties, and redox activity. *Angew. Chemie Int. Ed.* **2015,** *54* (1), 245-248.
12. Samuel, P. P.; Mondal, K. C.; Amin Sk, N.; Roesky, H. W.; Carl, E.; Neufeld, R.; Stalke, D.; Demeshko, S.; Meyer, F.; Ungur, L.; Chibotaru, L. F.; Christian, J.; Ramachandran, V.; van Tol, J.; Dalal, N. S., Electronic structure and slow magnetic relaxation of low-coordinate cyclic alkyl(amino) carbene stabilized iron(I) complexes. *J. Am. Chem. Soc.* **2014,** *136* (34), 11964-11971.
13. Errulat, D.; Harriman, K. L. M.; Gálico, D. A.; Ovens, J. S.; Mansikkamäki, A.; Murugesu, M., Aufbau vs. non-Aufbau ground states in two-coordinate d7 single-molecule magnets. *Inorg. Chem. Front.* **2021**.
14. Thomsen, M. K.; Nyvang, A.; Walsh, J. P. S.; Bunting, P. C.; Long, J. R.; Neese, F.; Atanasov, M.; Genoni, A.; Overgaard, J., Insights into Single-Molecule-Magnet Behavior from the Experimental Electron Density of Linear Two-Coordinate Iron Complexes. *Inorg. Chem.* **2019,** *58* (5), 3211-3218.
15. Werncke, C. G.; Suturina, E.; Bunting, P. C.; Vendier, L.; Long, J. R.; Atanasov, M.; Neese, F.; Sabo-Etienne, S.; Bontemps, S., Homoleptic Two-Coordinate Silylamido Complexes of Chromium(I), Manganese(I), and Cobalt(I). *Chem. Eur. J.* **2016,** *22* (5), 1668-1674.
16. Zadrozny, J. M.; Atanasov, M.; Bryan, A. M.; Lin, C.-Y.; Rekken, B. D.; Power, P. P.; Neese, F.; Long, J. R., Slow magnetization dynamics in a series of two-coordinate iron(ii) complexes. *Chem. Sci.* **2013,** *4* (1), 125-138.
17. Reiff, W. M.; LaPointe, A. M.; Witten, E. H., Virtual Free Ion Magnetism and the Absence of Jahn−Teller Distortion in a Linear Two-Coordinate Complex of High-Spin Iron(II). *J. Am. Chem. Soc.* **2004,** *126* (33), 10206-10207.
18. Goda, S.; Nikai, M.; Ito, M.; Hashizume, D.; Tamao, K.; Okazawa, A.; Kojima, N.; Fueno, H.; Tanaka, K.; Kobayashi, Y.; Matsuo, T., Synthesis and Magnetic Properties of Linear Two-coordinate Monomeric Diaryliron(II) Complexes Bearing Fused-ring Bulky “Rind” Groups. *Chemi. Lett.* **2016,** *45* (6), 634-636.
19. Merrill, W. A.; Stich, T. A.; Brynda, M.; Yeagle, G. J.; Fettinger, J. C.; De Hont, R.; Reiff, W. M.; Schulz, C. E.; Britt, R. D.; Power, P. P., Direct Spectroscopic Observation of Large Quenching of First-Order Orbital Angular Momentum with Bending in Monomeric, Two-Coordinate Fe(II) Primary Amido Complexes and the Profound Magnetic Effects of the Absence of Jahn− and Renner−Teller Distortions in Rigorously Linear Coordination. *J. Am. Chem. Soc.* **2009,** *131* (35), 12693-12702.
20. Atanasov, M.; Zadrozny, J. M.; Long, J. R.; Neese, F., A theoretical analysis of chemical bonding, vibronic coupling, and magnetic anisotropy in linear iron(ii) complexes with single-molecule magnet behavior. *Chem. Sci.* **2013,** *4* (1), 139-156.
21. Meng, Y. S.; Mo, Z. B.; Wang, B. W.; Zhang, Y. Q.; Deng, L.; Gao, S., Observation of the single-ion magnet behavior of d(8) ions on two-coordinate Co(I)-NHC complexes. *Chem. Sci.* **2015,** *6* (12), 7156-7162.
22. Poulten, R. C.; Page, M. J.; Algarra, A. G.; Le Roy, J. J.; López, I.; Carter, E.; Llobet, A.; Macgregor, S. A.; Mahon, M. F.; Murphy, D. M.; Murugesu, M.; Whittlesey, M. K., Synthesis, electronic structure, and magnetism of [Ni(6-Mes)2]+: a two-coordinate nickel(I) complex stabilized by bulky N-heterocyclic carbenes. *J. Am. Chem. Soc.* **2013,** *135* (37), 13640-13643.
23. Iglesias, M.; Beetstra, D. J.; Knight, J. C.; Ooi, L.-L.; Stasch, A.; Coles, S.; Male, L.; Hursthouse, M. B.; Cavell, K. J.; Dervisi, A.; Fallis, I. A., Novel Expanded Ring N-Heterocyclic Carbenes: Free

Carbenes, Silver Complexes, And Structures. *Organometallics* **2008,** *27* (13), 3279-3289.
24. Boatner, L. A.; Abraham, M. M., Electron paramagnetic resonance from actinide elements. *Rep. Prog. Phys.* **1978,** *41* (1), 87-155.
25. Mola, M.; Hill, S.; Goy, P.; Gross, M., Instrumentation for millimeter-wave magnetoelectrodynamic investigations of low-dimensional conductors and superconductors. *Rev. Sci. Instrum.* **1999,** *71* (1), 186-200.
26. Takahashi, S.; Hill, S., Rotating cavity for high-field angle-dependent microwave spectroscopy of low-dimensional conductors and magnets. *Rev. Sci. Instrum.* **2005,** *76* (2), 023114.
27. Ludwig, J.; Vasilyev, Y. B.; Mikhailov, N. N.; Poumirol, J. M.; Jiang, Z.; Vafek, O.; Smirnov, D., Cyclotron resonance of single-valley Dirac fermions in nearly gapless HgTe quantum wells. *Phys. Rev. B* **2014,** *89* (24), 241406.
28. Neese, F., Software update: the ORCA program system, version 4.0. *WIREs Comput. Mol. Sci.* **2018,** *8* (1), e1327.
29. Neese, F., The ORCA program system. *WIREs Comput. Mol. Sci.* **2012,** *2* (1), 73-78.
30. Weigend, F.; Ahlrichs, R., Balanced basis sets of split valence, triple zeta valence and quadruple zeta valence quality for H to Rn: Design and assessment of accuracy. *Phys. Chem. Chem. Phys.* **2005,** *7* (18), 3297-3305.
31. Aravena, D.; Neese, F.; Pantazis, D. A., Improved Segmented All-Electron Relativistically Contracted Basis Sets for the Lanthanides. *J. Chem. Theory Comput.* **2016,** *12* (3), 1148-1156.
32. Jung, J.; Atanasov, M.; Neese, F., Ab Initio Ligand-Field Theory Analysis and Covalency Trends in Actinide and Lanthanide Free Ions and Octahedral Complexes. *Inorg. Chem.* **2017,** *56* (15), 8802-8816.
33. Rieger, P. H., Electron paramagnetic resonance studies of low-spin d5 transition metal complexes. *Coord. Chem. Rev.* **1994,** *135-136*, 203-286.
34. McGarvey, B. R., Survey of ligand field parameters of strong field d5 complexes obtained from the g matrix. *Coord. Chem. Rev.* **1998,** *170* (1), 75-92.
35. Krishnamurthy, R.; Schaap, W. B., Computing ligand field potentials and relative energies of d orbitals: A simple general approach. *J. Chem. Educ.* **1969,** *46* (12), 799.
36. Wagner, C. L.; Tao, L.; Fettinger, J. C.; Britt, R. D.; Power, P. P., Two-coordinate, late first-row transition metal amido derivatives of the bulky ligand -N(SiPri3)Dipp (Dipp = 2,6-diisopropylphenyl): effects of the ligand on the stability of two-coordinate copper(II) complexes. *Inorg. Chem.* **2019,** *58* (13), 8793-8799.
37. Samuel, P. P.; Mondal, K. C.; Roesky, H. W.; Hermann, M.; Frenking, G.; Demeshko, S.; Meyer, F.; Stückl, A. C.; Christian, J. H.; Dalal, N. S.; Ungur, L.; Chibotaru, L. F.; Pröpper, K.; Meents, A.; Dittrich, B., Synthesis and characterization of a two-coordinate manganese complex and its reaction with molecular hydrogen at room temperature. *Angew. Chemie Int. Ed.* **2013,** *52* (45), 11817-11821.
38. Reta, D.; Chilton, N. F., Uncertainty estimates for magnetic relaxation times and magnetic relaxation parameters. *Phys. Chem. Chem. Phys.* **2019,** *21* (42), 23567-23575.
39. Lunghi, A.; Totti, F.; Sessoli, R.; Sanvito, S., The role of anharmonic phonons in under-barrier spin relaxation of single molecule magnets. *Nat. Commun.* **2017,** *8* (1), 14620.
40. Lunghi, A.; Totti, F.; Sanvito, S.; Sessoli, R., Intra-molecular origin of the spin-phonon coupling in slow-relaxing molecular magnets. *Chem. Sci.* **2017,** *8* (9), 6051-6059.
41. Lunghi, A.; Sanvito, S., How do phonons relax molecular spins? *Sci. Adv.* **2019,** *5* (9), eaax7163.
42. Albino, A.; Benci, S.; Tesi, L.; Atzori, M.; Torre, R.; Sanvito, S.; Sessoli, R.; Lunghi, A., First-principles investigation of spin–phonon coupling in vanadium-based molecular spin quantum bits. *Inorg. Chem.* **2019,** *58* (15), 10260-10268.
43. Briganti, M.; Santanni, F.; Tesi, L.; Totti, F.; Sessoli, R.; Lunghi, A., A Complete Ab Initio View of Orbach and Raman Spin–Lattice Relaxation in a Dysprosium Coordination Compound. *J. Am. Chem. Soc.* **2021,** *143* (34), 13633-13645.

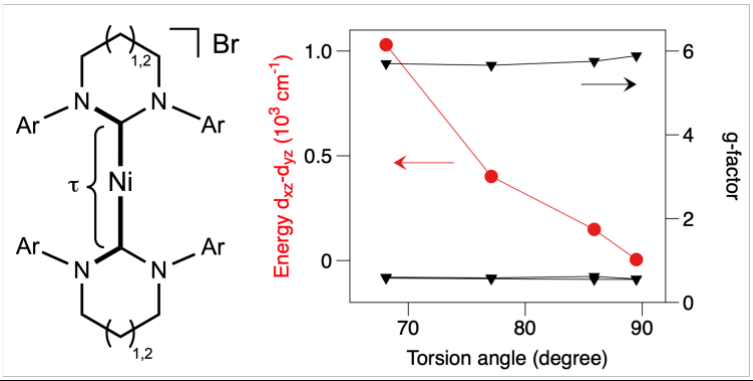

A series of new Ni(I) bis-N-heterocyclic carbene complexes with extremely anisotropic g-tensors show no correlation between magnetic properties and the torsion angle between the two ligands despite significant changes in the *d*-orbitals splitting.

Supporting Information

Extreme g-tensor anisotropy and its insensitivity to structural distortions in a family of linear two-coordinate Ni(I) bis-N-heterocyclic carbene complexes

William J. M. Blackaby[1], Katie L. M. Harriman[2], Samuel M. Greer[3,4], Andrea Folli[6], Stephen Hill[3,5], Vera Krewald[7], Mary F. Mahon[1], Damien M. Murphy[6], Muralee Murugesu[2], Emma Richards[6*], Elizaveta Suturina[1*] and Michael K. Whittlesey[1]

[1]Department of Chemistry, University of Bath, Claverton Down, Bath BA2 7AY, U. K.

[2]Department of Chemistry and Biomolecular Sciences, University of Ottawa, 10 Marie Curie, Ottawa, Ontario K1N 6N5, Canada

[3]National High Magnetic Field Laboratory, Florida State University, Tallahassee, FL 32310, United States

[4]Department of Chemistry, Florida State University, Tallahassee, FL 32306, United States.

[5]Department of Physics, Florida State University, Tallahassee, FL 32306, United States.

[6]School of Chemistry, Cardiff University, Park Place, Cardiff CF10 3AT, U. K.

[7]Theoretical Chemistry, TU Darmstadt, Alarich-Weiss-Strasse 4, 64287 Darmstadt, Germany

Corresponding Authors

Emma Richards - School of Chemistry, Cardiff University, Park Place, Cardiff CF10 3AT, U.K.
Email: RichardsE10@cardiff.ac.uk
https://orcid.org/0000-0001-6691-2377

Elizaveta Suturina - Department of Chemistry, University of Bath, Claverton Down, Bath BA2 7AY, U.K.
Email: e.suturina@bath.ac.uk
https://orcid.org/0000-0003-4407-1882

Synthesis and general procedures

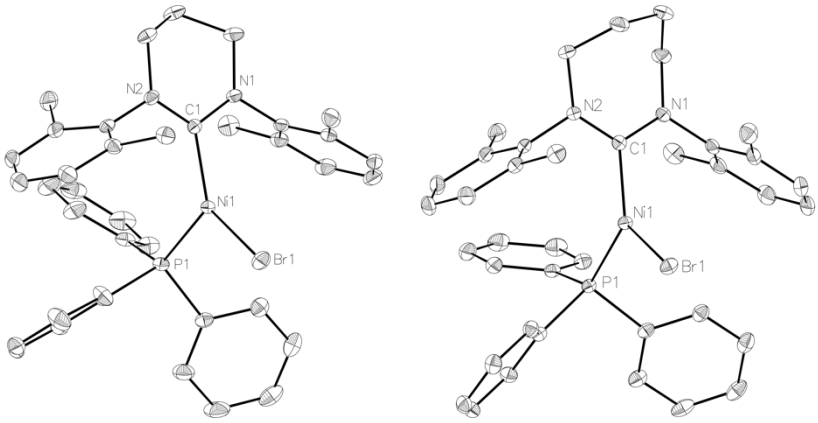

Figure S 1. Molecular structures of (left) Ni(6Xyl)(PPh$_3$)Br and (right) Ni(7Xyl)(PPh$_3$)Br. Hydrogen atoms and solvent moieties have been omitted for clarity in these plots, as has the minor disordered component Ni(6Xyl)(PPh$_3$)Br. Ellipsoids are represented at 30% probability, throughout.

X-Ray diffraction

CCDC 2083185-2083189 contain the supplementary crystallographic data for **2-6Xyl**, **2-7Mes**, **2-7Xyl**, [Ni(6Xyl)(PPh$_3$)Br] and [Ni(7Xyl)(PPh$_3$)Br]. These data can be obtained free of charge from The Cambridge Crystallographic Data Centre via www.ccdc.cam.ac.uk/structures.

Table S 1. Crystal structure refinement parameters.

Identification code	**[2-6Xyl]**	**[2-7Mes]**	**[2-7Xyl]**	**Ni(6Xyl)(PPh$_3$)Br**	**Ni(7Xyl)(PPh$_3$)Br**
Empirical formula	$C_{42}H_{52}N_4NiBrCl_4$	$C_{47}H_{62}BrCl_2N_4Ni$	$C_{44}H_{56}N_4Cl_4NiBr$	$C_{38}H_{39}BrN_2NiP$	$C_{48}H_{50}BrN_2NiP$
Formula weight	893.29	892.52	921.34	693.30	824.49
Temperature/K	150.00(10)	150.01(10)	149.9(3)	150.02(11)	150.00(10)
Crystal system	monoclinic	orthorhombic	monoclinic	triclinic	monoclinic
Space group	*C*2/*c*	*Pca*2$_1$	*C*2/*c*	*P*–1	*P*2$_1$/*n*
a/ Å	15.41478(14)	17.55756(9)	15.7903(3)	10.0658(3)	9.9401(2)
b/ Å	13.97716(11)	12.09149(6)	13.6094(2)	10.4271(3)	23.4907(4)
c/ Å	20.40543(19)	21.14171(10)	21.2365(5)	16.3374(4)	17.9641(4)
α/ °	90	90	90	90.258(2)	90
β/ °	105.2482(10)	90	105.989(2)	92.694(3)	105.451(2)
γ/ °	90	90	90	107.240(3)	90
U/ Å^3	4241.67(7)	4488.32(4)	4387.11(16)	1635.57(9)	4043.01(16)
Z	4	4	4	2	4
ρ_{calc}/ g cm^{-3}	1.399	1.321	1.395	1.408	1.355
μ/ mm^{-1}	4.340	3.030	1.632	1.893	1.544
F(000)	1852.0	1876.0	1916.0	718.0	1720.0
Crystal size/ mm^3	0.265 × 0.207 × 0.16	0.264 × 0.152 × 0.088	0.332 × 0.278 × 0.203	0.456 × 0.365 × 0.167	0.407 × 0.301 × 0.257
Radiation	CuKα (λ = 1.54184)	CuKα (λ = 1.54184)	MoKα (λ = 0.71073)	MoKα (λ = 0.71073)	MoKα (λ = 0.71073)
2θ range for data collection/°	8.682 to 144.904	7.31 to 145.032	6.57 to 54.968	6.518 to 54.958	6.72 to 54.964
Index ranges	–15 ≤ h ≤ 19, –17 ≤ k ≤ 17, –25 ≤ l ≤ 25	–21 ≤ h ≤ 21, –14 ≤ k ≤ 14, –26 ≤ l ≤ 19	–20 ≤ h ≤ 20, –17 ≤ k ≤ 17, –27 ≤ l ≤ 27	–13 ≤ h ≤ 13, –13 ≤ k ≤ 13, –21 ≤ l ≤ 21	–11 ≤ h ≤ 12, –30 ≤ k ≤ 30, –23 ≤ l ≤ 23
Reflections collected	22050	57741	21856	54485	39111
Independent reflections, R_{int}	4197, 0.0203	6924, 0.0345	5036, 0.0261	7496, 0.0364	9249, 0.0335
Data/restraints/parameters	4197/0/240	6924/1/508	5036/0/249	7496/96/466	9249/0/482
Goodness–of–fit on F^2	1.022	1.033	1.038	1.062	1.041
Final *R*1, *wR*2 [*I*>=2σ(*I*)]	0.0381, 0.0927	0.0308, 0.0821	0.0287, 0.0716	0.0294, 0.0695	0.0345, 0.0804
Final *R*1, *wR*2 [all data]	0.0392, 0.0934	0.0315, 0.0827	0.0401, 0.0774	0.0394, 0.0739	0.0488, 0.0873
Largest diff. peak/hole/ e Å^{-3}	1.02/–1.02	0.72/–0.53	0.45/–0.48	0.47/–0.31	0.86/–0.63
Flack parameter	–	–0.255(13)	–	–	–

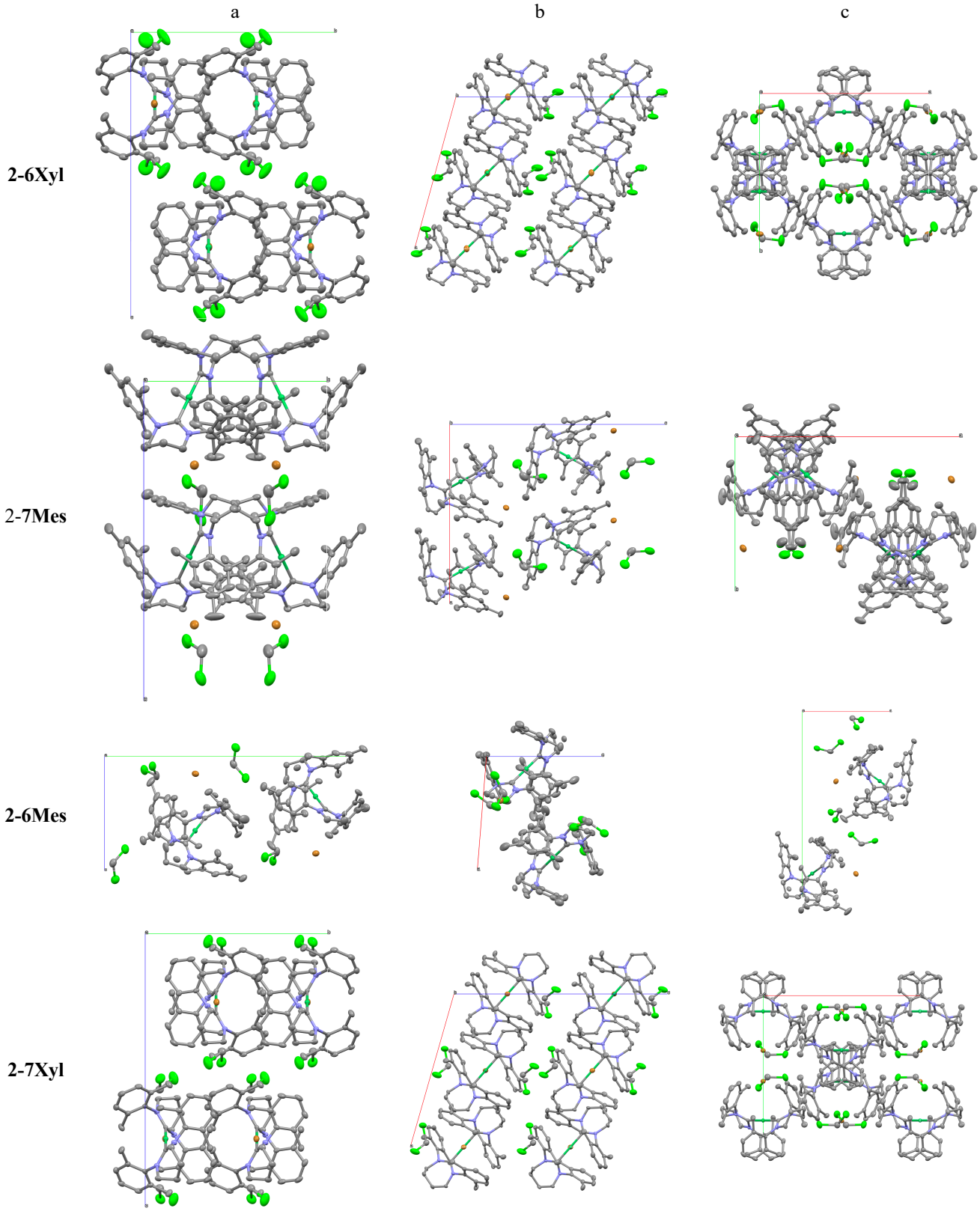

Figure S 2. Unit cell view along main crystallographic axes demonstrating differences in the packing.

NMR spectra and analysis

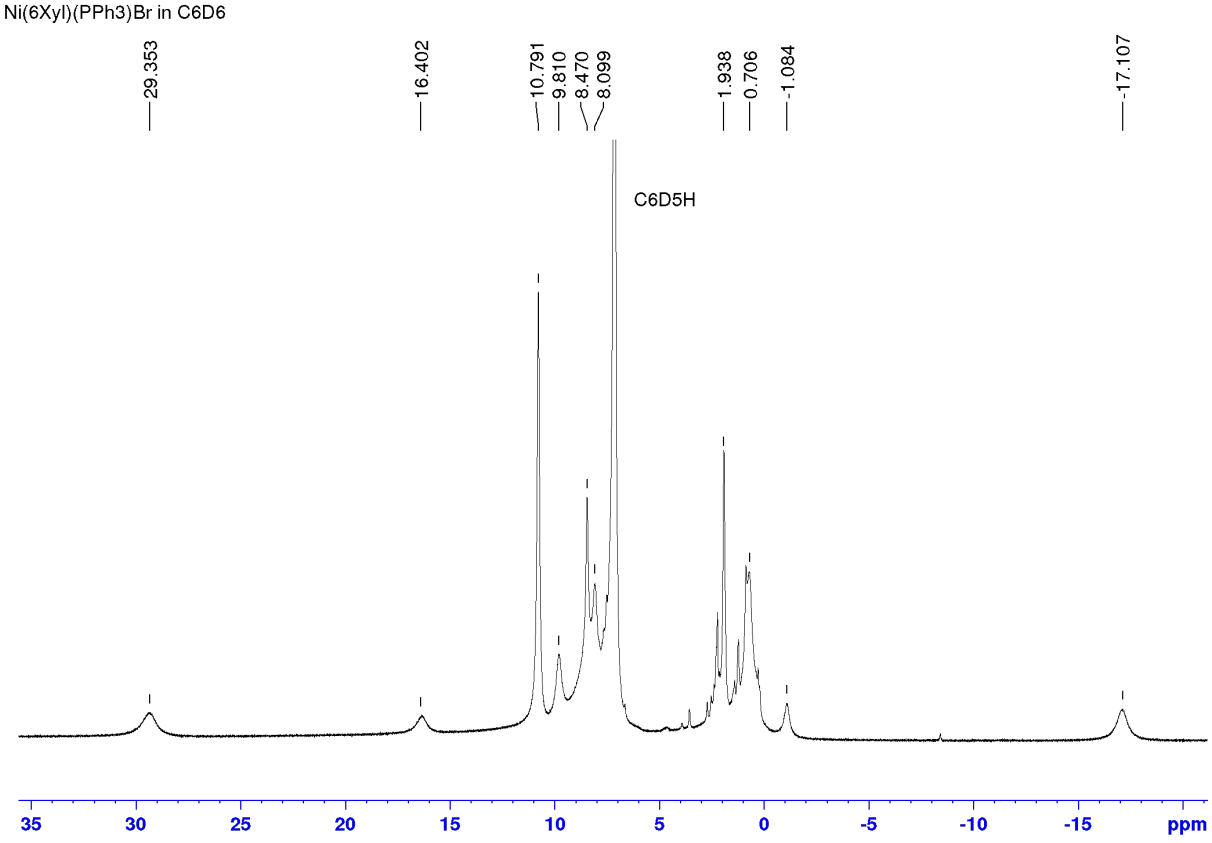

Figure S 3. ^{1}H NMR spectrum of Ni(6Xyl)(PPh_3)Br (C_6D_6, 500 MHz, 298 K).

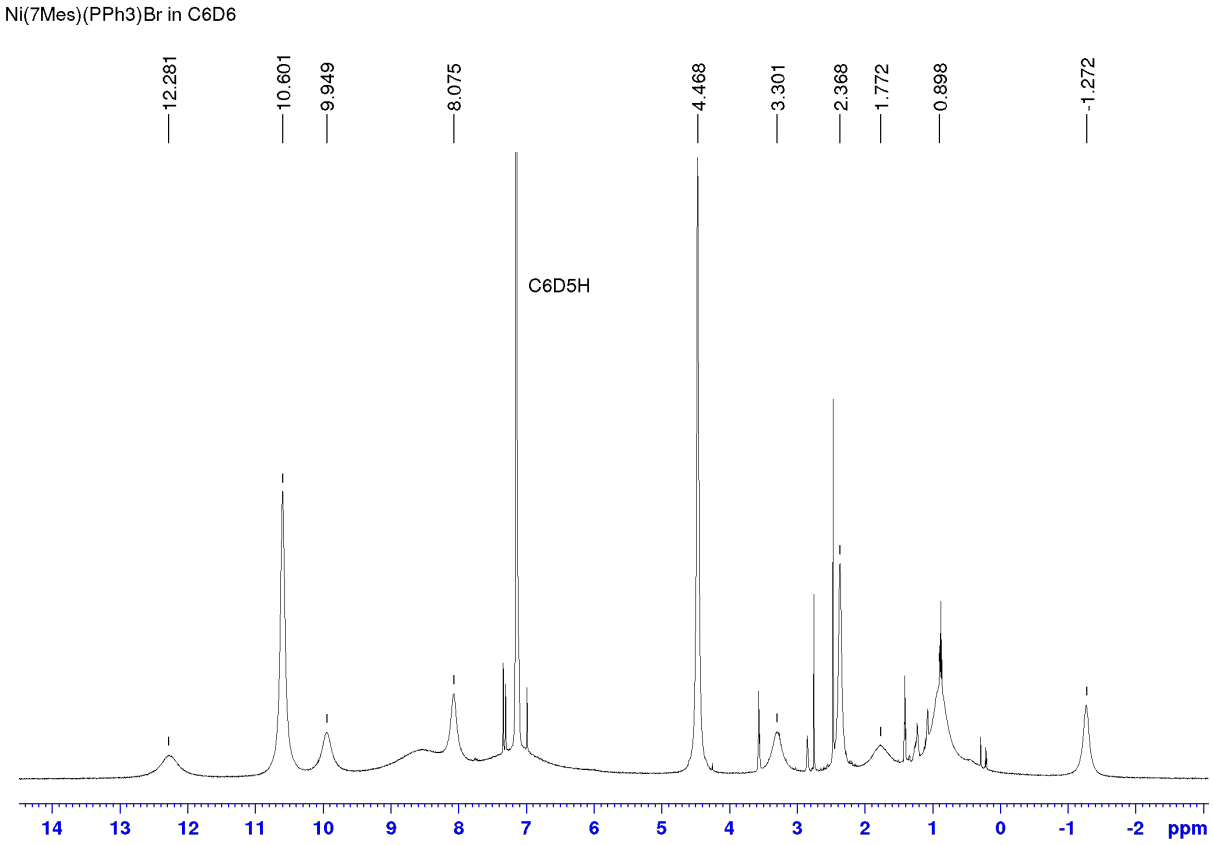

Figure S 4. ^{1}H NMR spectrum of Ni(7Mes)(PPh$_3$)Br (C_6D_6, 500 MHz, 298 K).

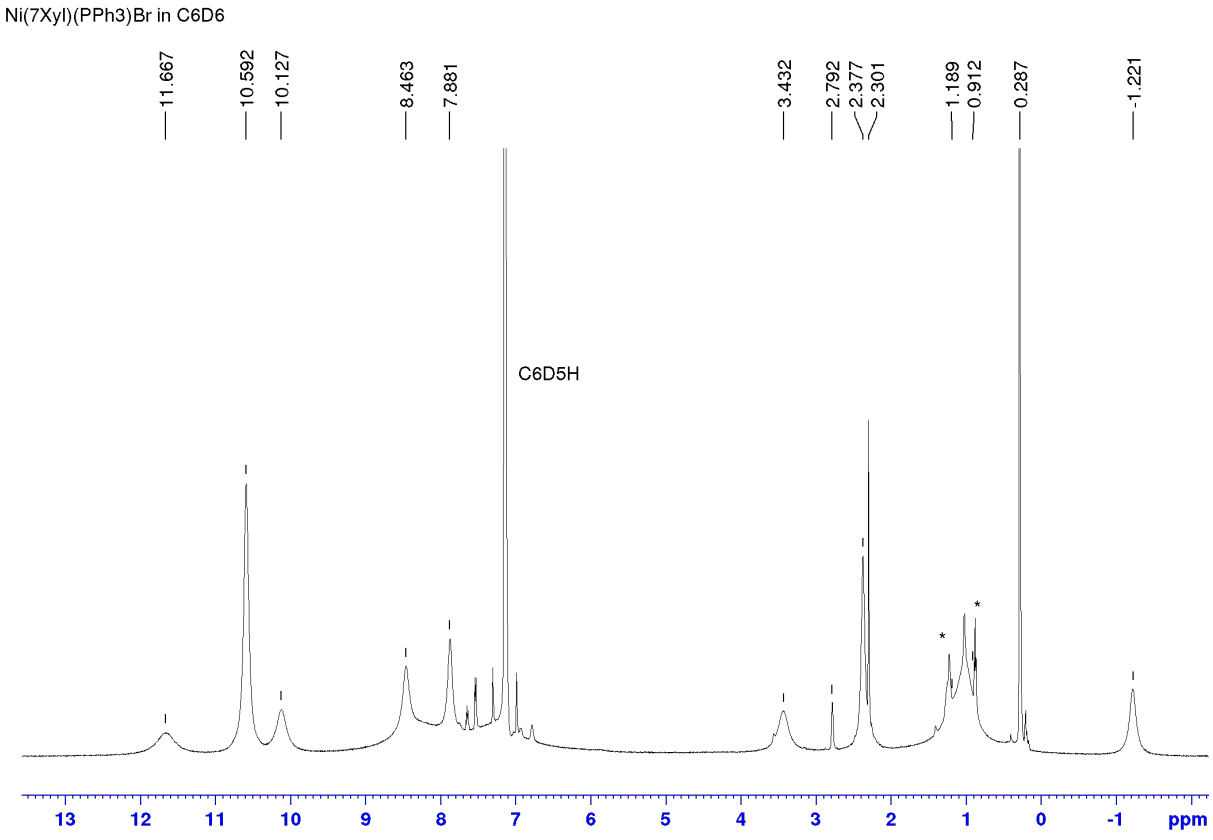

*Figure S 5. ^{1}H NMR spectrum of Ni(7Xyl)(PPh$_3$)Br (C_6D_6, 500 MHz, 298 K; * = hexane).*

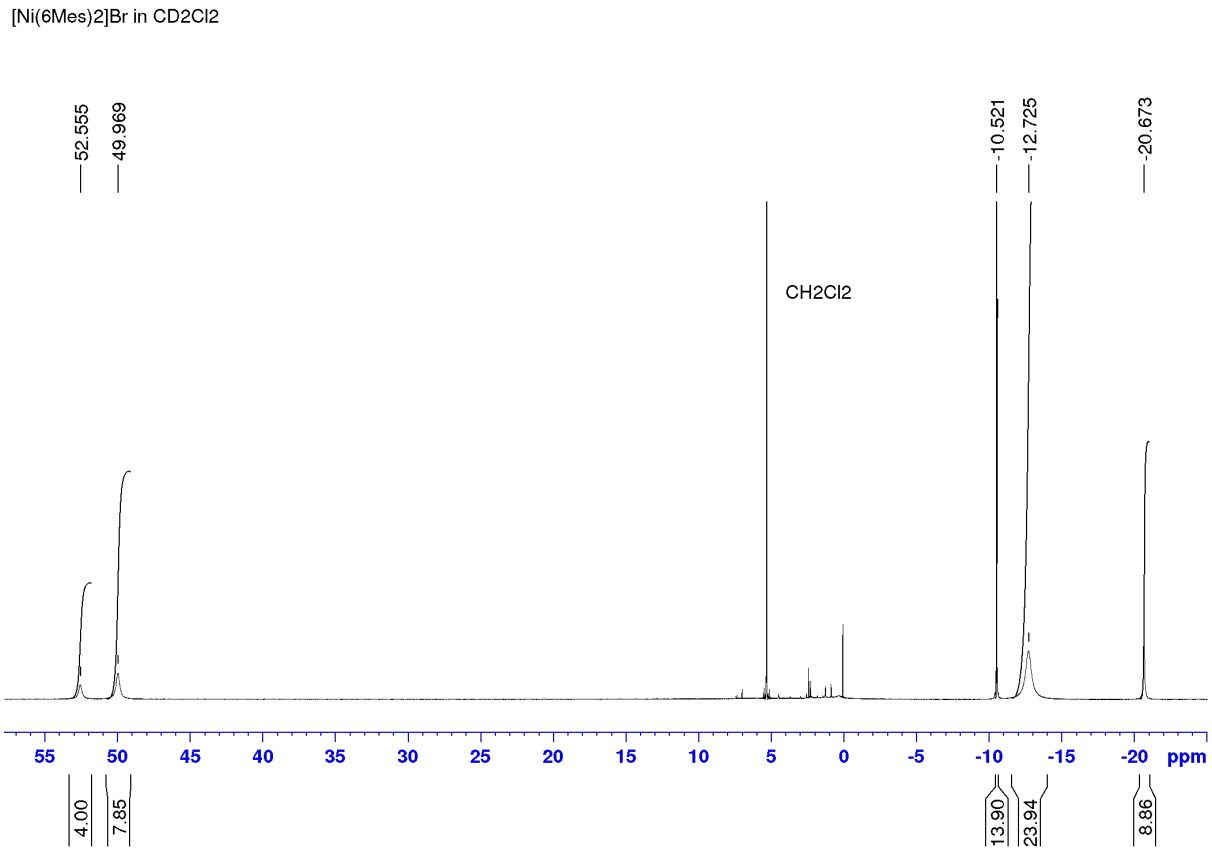

*Figure S 6. ^{1}H NMR spectrum of **[2-6Mes]** (CD_2Cl_2, 400 MHz, 298 K).*

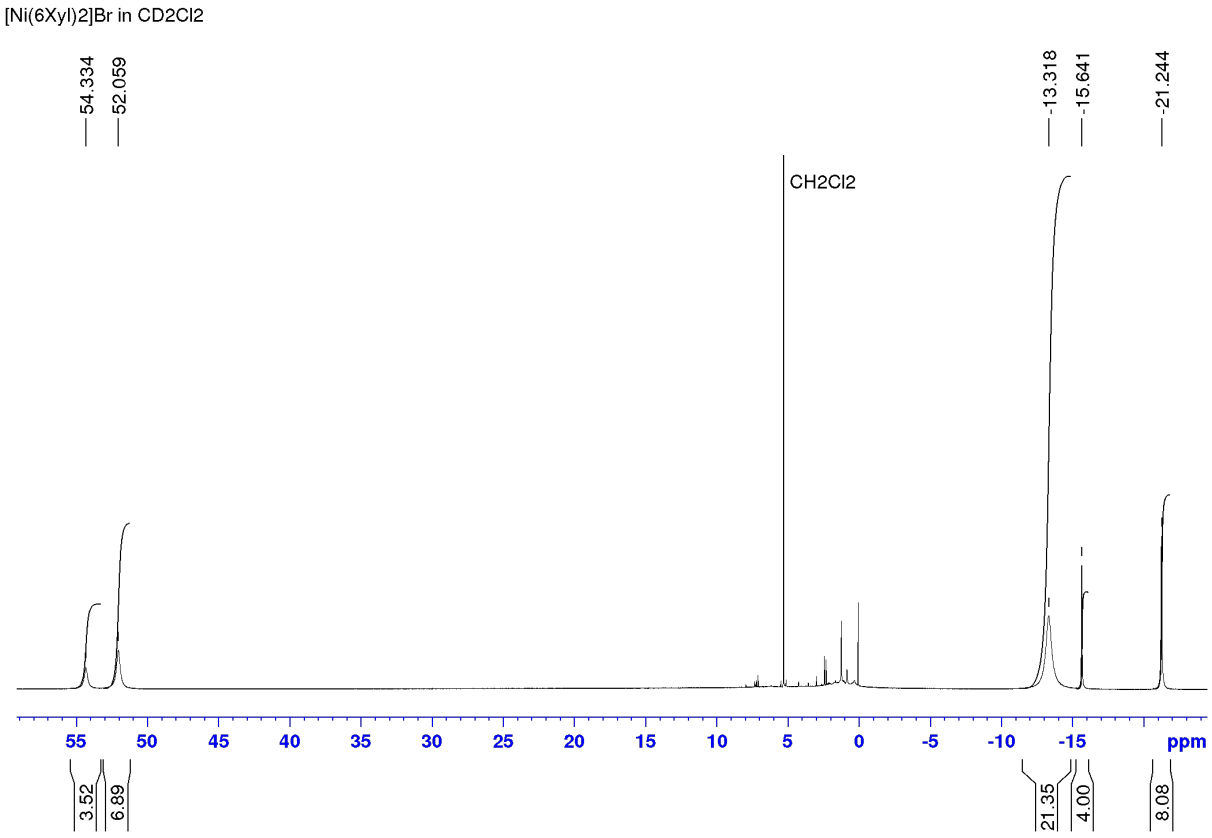

*Figure S 7. ^{1}H NMR spectrum of **[2-6Xyl]** (CD_2Cl_2, 500 MHz, 298 K).*

[Ni(7Mes)2]Br in CD2Cl2

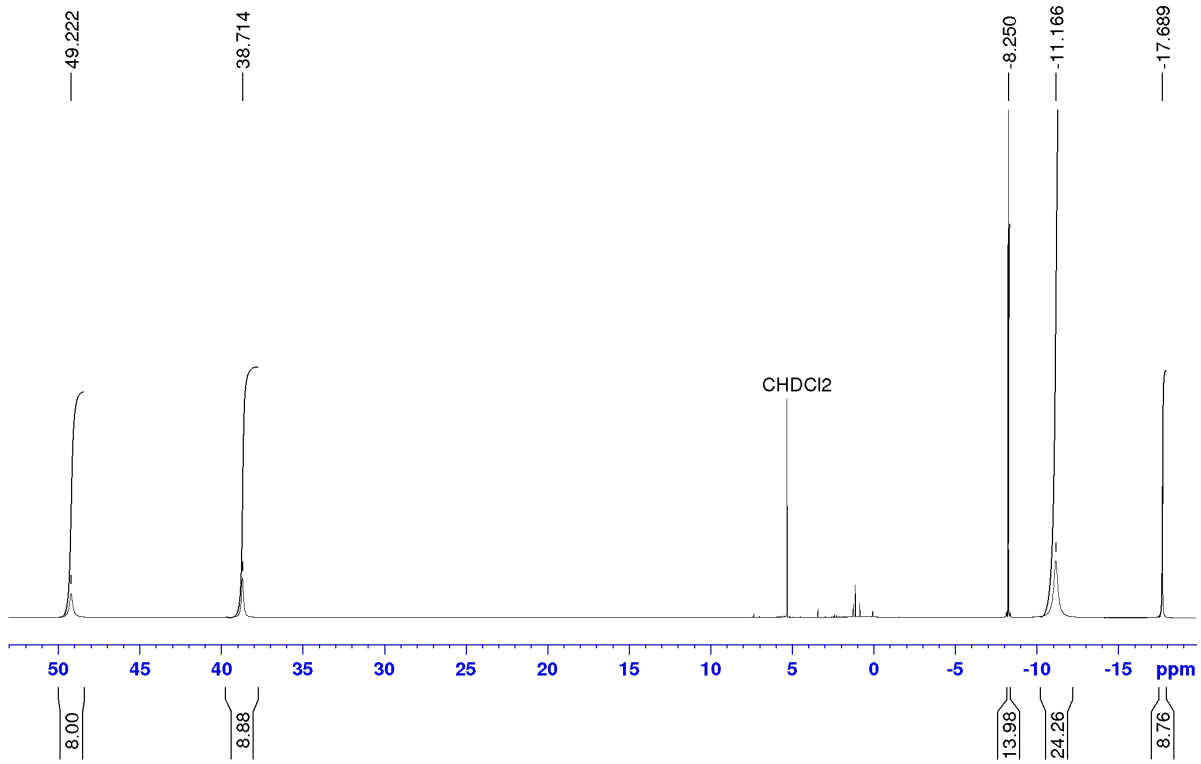

*Figure S 8. ^{1}H NMR spectrum of **[2-7Mes]** (CD_2Cl_2, 500 MHz, 298 K).*

[Ni(7Xyl)2]Br in CD2Cl2

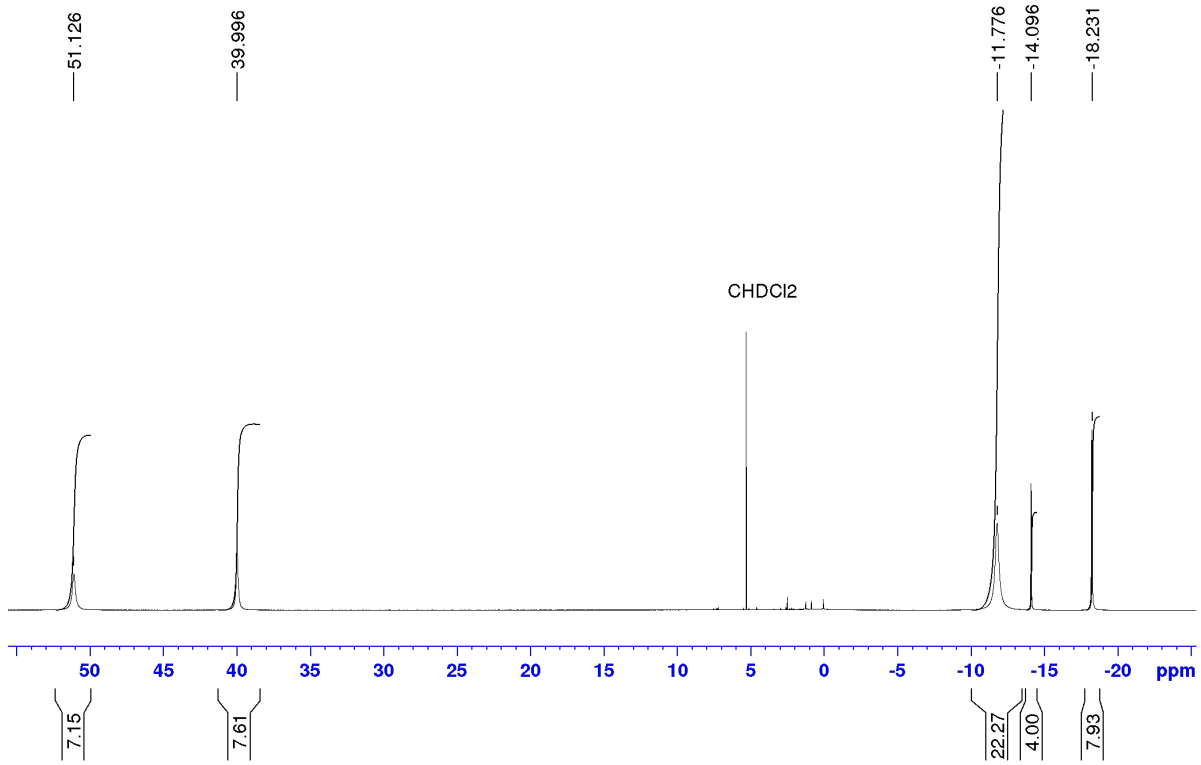

*Figure S 9. ^{1}H NMR spectrum of **[2-7Xyl]** (CD_2Cl_2, 500 MHz, 298 K).*

NMR analysis

Paramagnetic NMR shifts were assigned based on DFT (B3LYP/def2-TZVP) calculated hyperfine tensors. The paramagnetic shift was then used to extract the magnetic susceptibility tensor with a linear least squares fit.

$$\delta = \left(A_{iso}\chi_{iso} + A_{ax}\Delta\chi_{ax} \right) \frac{10^{-28}}{\gamma_N \hbar \mu_0}$$

where $A_{iso} = \left(A_{xx} + A_{yy} + A_{zz} \right) / 3$ and $A_{ax} = \left(2A_{zz} - A_{xx} - A_{yy} \right) / 9$ are taken in units of Gauss from DFT calculation. A fit that accounted for both contact and pseudocontact (PCS) contributions showed that the contact contributions are much smaller than PCS and that it is impossible to extract χ_{iso} based on just 5 observed proton peaks. To eliminate overparameterization only PCS was fitted.

Table S 2. Axiality of the magnetic susceptibility tensor in Å³ ESI extracted from the room temperature NMR shifts and computed with SOC-CASSCF/NEVPT2

	$\Delta\chi_{ax}$ (Å ^{3})		
	from NMR	from NEVPT2 on optimised geometry	from NEVPT2 on X-Ray geometry
2-6Mes	0.15(1)	0.20	0.21
2-6Xyl	0.15(1)	0.18	0.21
2-7Mes	0.13(1)	0.20	0.19
2-7Xyl	0.14(1)	0.20	0.21

Computed and NMR extracted anisotropy of the magnetic susceptibility agrees reasonably well. It should be noted that we assumed fast exchange for all mobile groups while fitting.
The main magnetic axis was set to align with the Ni-C bond. The total PCS field shown for **2-7Mes** is shown below.

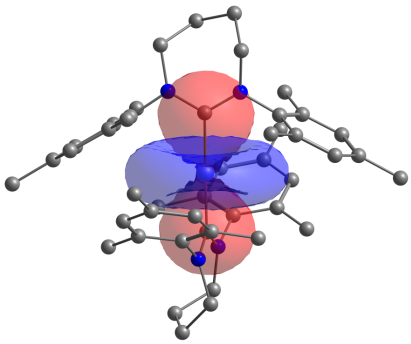

Figure S 10. Iso-surface (±100 ppm) of pseudocontact shift showing that positive shift (red) is expected for CH_2 groups and negative (blue) for phenyl groups.

SQUID magnetometry

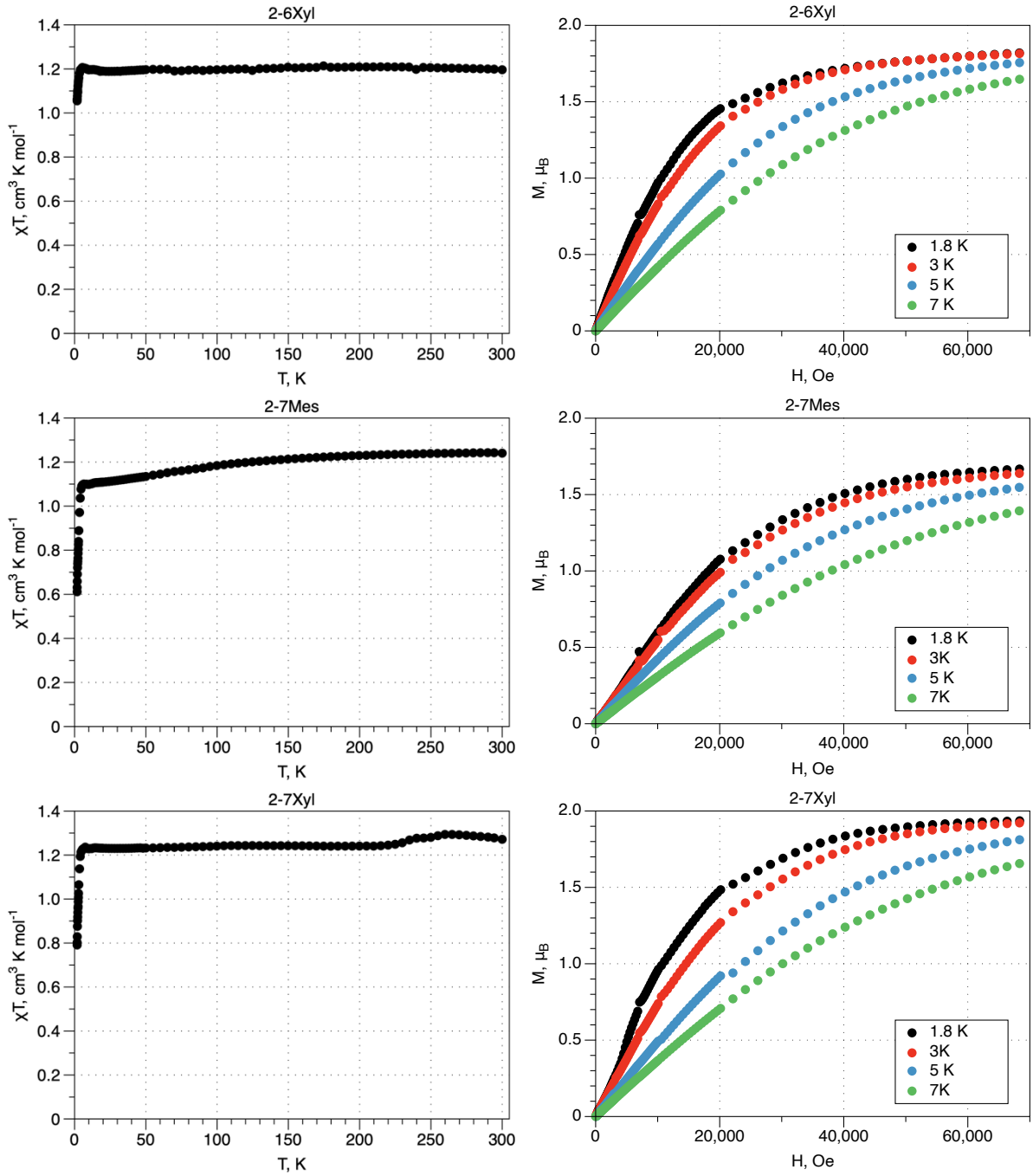

*Figure S 11. Temperature dependence of the χT product under a 1000 Oe applied dc field (left) and magnetic field dependence of the magnetization (right) measured for crushed polycrystalline samples of **2-6Xyl**, **2-7Mes** and **2-7Xyl** from top to bottom respectively.*

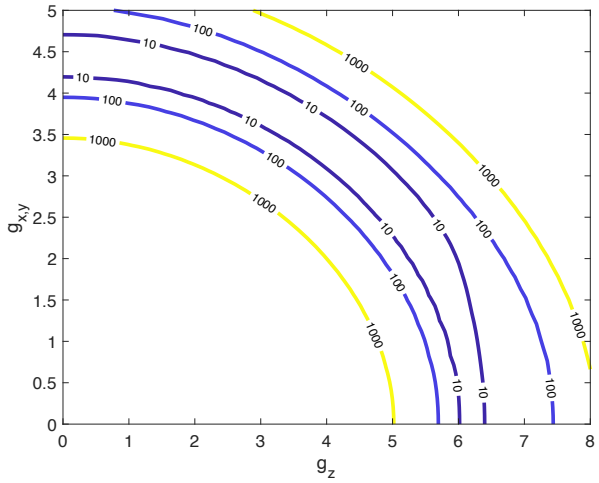

*Figure S 12. Error plot for the fit of the magnetization and susceptibility data of **2-6Xyl** showing the dependence of the best-fit $g_{\parallel}$ (g_z) and $g_{\perp}$ ($g_{x,y}$) values.*

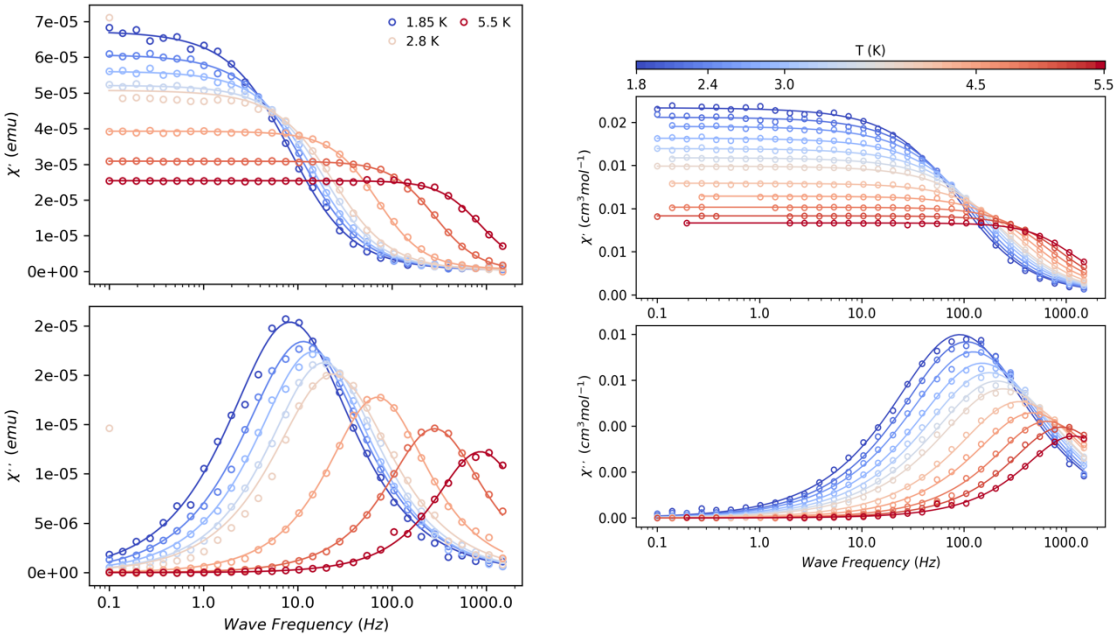

2-7Mes **2-7Xyl**

Figure S 13. Frequency dependence of the in-phase (χ'; top) and out-of-phase (χ''; bottom) ac magnetic susceptibility under an applied static field, H_{dc} = 600 Oe (circles) and best fits to the generalised Debye model (lines) obtained with CC-FIT2[1].

Electron Paramagnetic Resonance

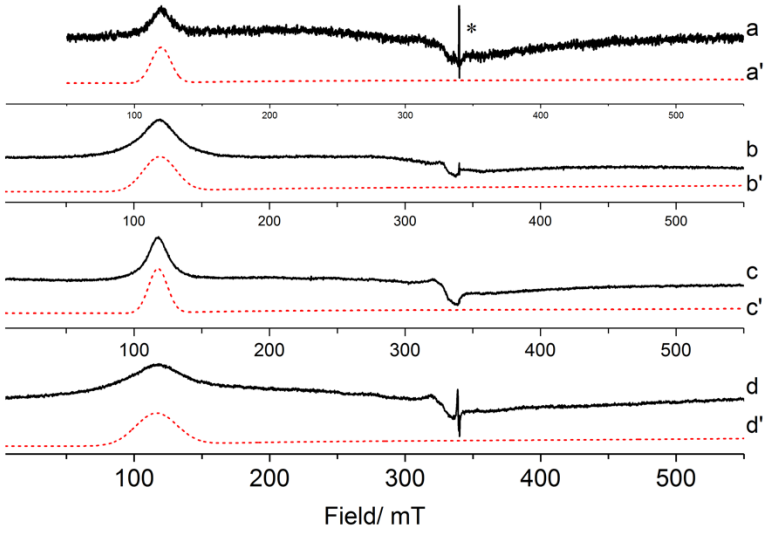

*Figure S 14. Experimental (solid black) X-band CW EPR spectra of (a) **2-6Mes**, (b) **2-7Mes**, (c) **2-6Xyl**,, and (d) **2-7Xyl**, in frozen DCM solution at 140 K. Corresponding simulations are shown in a′- d′(dashed red). Cavity artefacts and impurities in the quartz tube are marked with an asterisk ∗.*

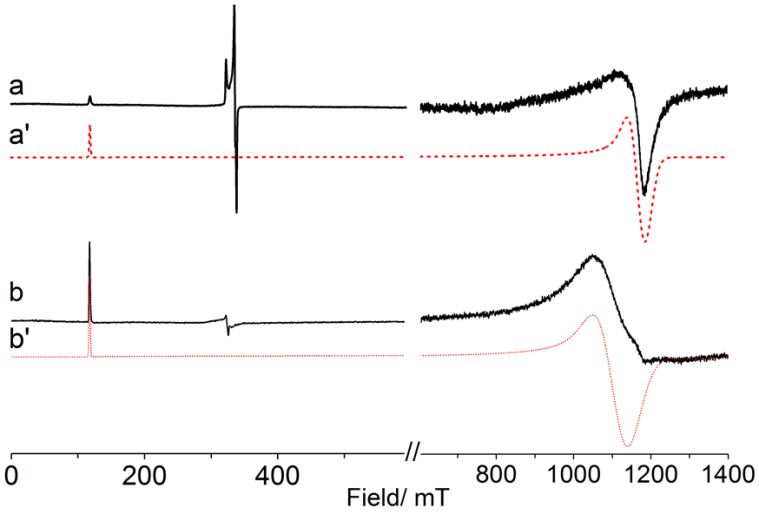

*Figure S 15. Experimental (solid black) X-band CW EPR spectra of (a) **2-6Mes**, and (b) **2-7Xyl**,, in frozen DCM solution at 10 K. Corresponding simulations are shown in a′ and b′ (dashed red). The signal at ~320 mT is attributed to a paramagnetic impurity.*

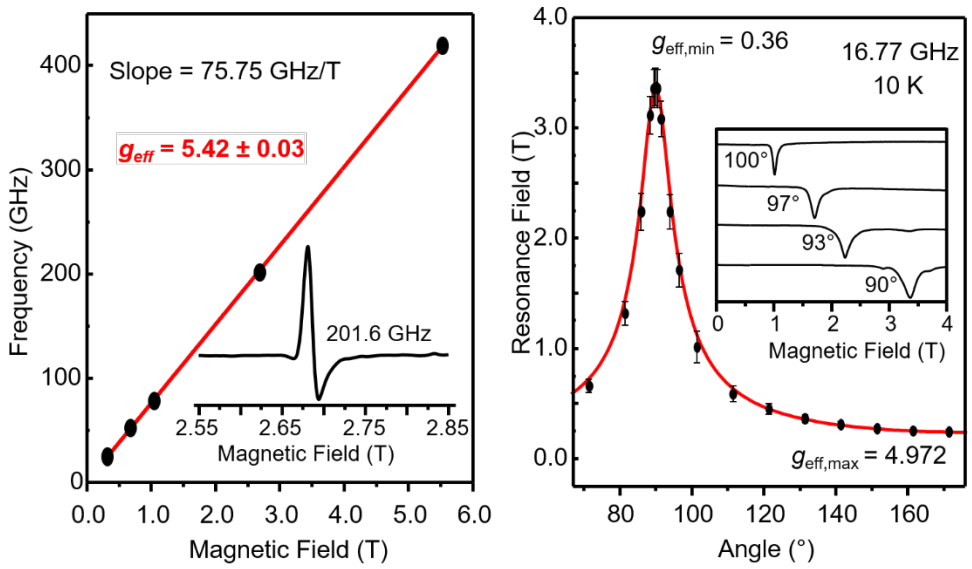

*Figure S 16. a) Two-dimensional frequency vs resonant field plot of the observed EPR transitions for a powder sample of **2-6Mes**. Black circles represent the experimentally observed resonance positions while the red line shows the least squares fit to the data. The inset shows a typical example spectrum. The slight derivative shape is likely an indication of some alignment of the microcrystallites with the applied field. b) Resonance field vs probe angle plot of the observed EPR transitions for a single crystal of **2-6Mes**. The red line shows the expected for $g_{||}$ = 5.42, $g_{\perp}$ = 0.36, rotated about an axis ~70° from the $g_{||}$ direction. The inset shows a series of spectra recorded at various angles.*

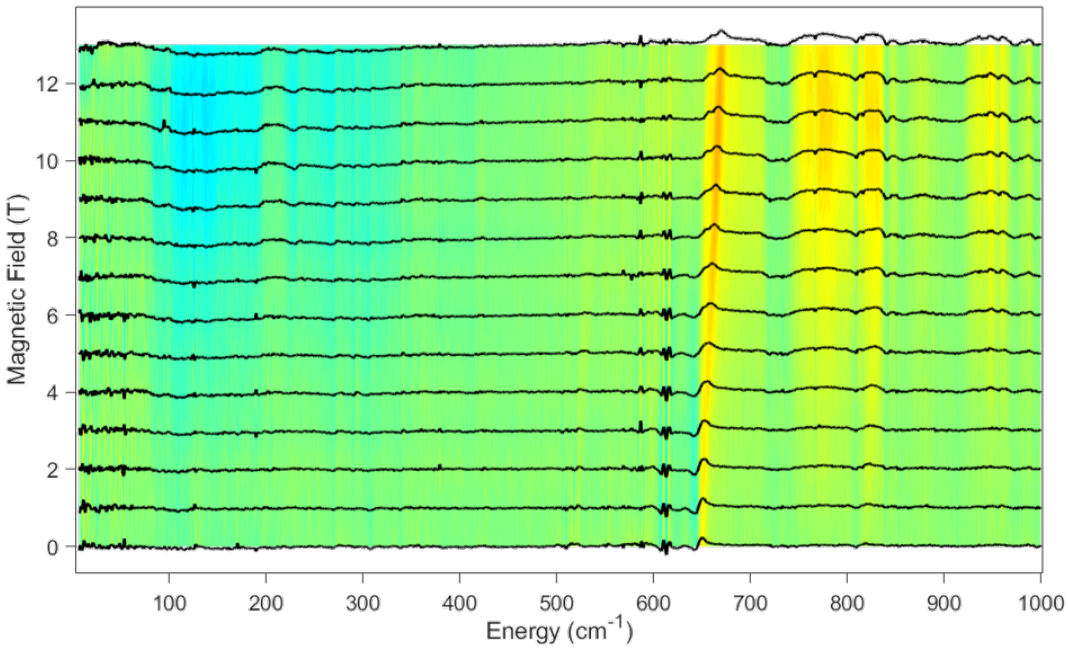

*Figure S 17. FTIR spectra of **2-6Mes** divided by reference spectra recorded at 4 T larger field. Each trace is offset by the applied magnetic field. The bottom surface is a 2D color plot.*

Crystal Field Model for the Analysis EPR and FIRMS Results

To model the reduction of $g_{||}$ from the maximum value, 6, we must consider the effect of the ligand field. Starting in the familiar basis of the real orbitals we can define a ligand field interaction ($\hat{V}_{LF}$) given by:

$$\hat{V}_{LF} = \begin{matrix} x^2\text{-}y^2 & xy \end{matrix} \begin{bmatrix} -\delta & \Delta \\ \Delta & +\delta \end{bmatrix},$$

where 2δ is equal to the energy separation between x^2-y^2/xy orbitals and defined in the matrix such that the average orbital energy is zero and Δ is a mixing parameter.

Since we are primarily interested in the effects of spin-orbit coupling and the applied magnetic field, it is convenient to work in the M_L basis where both operators are diagonal. The real and M_L orbitals are related by rotation ($\overleftrightarrow{T}_{\text{real}\rightarrow M_L}$) and, therefore:

$$\hat{V}_{LF,M_L} = \overleftrightarrow{T}_{\text{real}\rightarrow M_L} \cdot \hat{V}_{LF,real} \cdot \overleftrightarrow{T}_{\text{real}\rightarrow M_L}^{\dagger},$$

where,

$$\overleftrightarrow{T}_{\text{real}\rightarrow M_L} = \frac{1}{\sqrt{2}} \begin{bmatrix} 1 & -i \\ 1 & i \end{bmatrix}.$$

Therefore,

$$\hat{V}_{LF,M_L} = \begin{matrix} +2 & -2 \end{matrix} \begin{bmatrix} 0 & -\delta - i\Delta \\ -\delta + \Delta & 0 \end{bmatrix}.$$

To make this ligand field potential, which is currently in an orbital basis set, compatible with the spin-orbit coupling operator we must expand it to include spin. Since the crystal field potential does not act on S this can be done by taking the Kronecker product of V_{LF,M_L} with the identity matrix, resulting in:

$$\hat{V}_{LF,M_L} = \begin{matrix} +2\alpha & -2\alpha & +2\beta & -2\beta \end{matrix} \begin{bmatrix} 0 & -\delta - i\Delta & 0 & 0 \\ -\delta + \Delta & 0 & 0 & 0 \\ 0 & 0 & 0 & -\delta - i\Delta \\ 0 & 0 & -\delta + \Delta & 0 \end{bmatrix}.$$

In this simplified two orbital model the spin-orbit coupling Hamiltonian, $\hat{H}_{SOC}$, is given by:

$$\hat{H}_{SOC} = \frac{\zeta}{2S} \hat{L}_z \hat{S}_z,$$

$$= \begin{matrix} +2\alpha & -2\alpha & +2\beta & -2\beta \end{matrix} \begin{bmatrix} -\zeta & 0 & 0 & 0 \\ 0 & +\zeta & 0 & 0 \\ 0 & 0 & +\zeta & 0 \\ 0 & 0 & 0 & -\zeta \end{bmatrix}$$

where ζ is the one electron spin – orbit coupling constant. Lastly the Zeeman interaction operator, $\hat{H}_{Z,\mu}$, is given by:

$$\hat{H}_{Z,\mu} = \beta_e B_\mu \left(\hat{L}_\mu + g_e \hat{S}_\mu \right),$$

$$= \begin{array}{c} \begin{matrix} +2\alpha & -2\alpha & +2\beta & -2\beta \end{matrix} \\ \begin{bmatrix} 3\beta_e B_{||} & \beta_e B_\perp & 0 & 0 \\ \beta_e B_\perp & -\beta_e B_{||} & 0 & 0 \\ 0 & 0 & \beta_e B_{||} & -\beta_e B_\perp \\ 0 & 0 & -\beta_e B_\perp & -3\beta_e B_{||} \end{bmatrix} \end{array},$$

where β_e is the electronic Bohr magneton, μ represents the cartesian component, and B_μ is the applied magnetic field such that $B_{x,y} = B_\perp$ and $B_z = B_{||}$. The total Hamiltonian can then be expressed as:

$$\hat{H}_{Total} = \hat{V}_{LF,M_L} + \hat{H}_{SOC} + \hat{H}_Z,$$

$$= \begin{array}{c} \begin{matrix} +2\alpha & -2\alpha & +2\beta & -2\beta \end{matrix} \\ \begin{bmatrix} 3\beta_e B_{||} - \zeta & \beta_e B_\perp - \delta - i\Delta & 0 & 0 \\ \beta_e B_\perp - \delta + i\,\Delta & -\beta_e B_{||} + \zeta & 0 & 0 \\ 0 & 0 & \beta_e B_{||} + \zeta & -\beta_e B_\perp - \delta - i\Delta \\ 0 & 0 & -\beta_e B_\perp - \delta + i\Delta & -3\beta_e B_{||} - \zeta \end{bmatrix} \end{array}$$

From here we can derive an analytical expression for $g_{||}$ by setting $B_\perp = 0$ and finding the lowest energy eigenvalue of the block diagonal matrix:

$$E_{1,||} = -\beta_e B_{||} + \sqrt{4{\beta_e}^2 B_{||}^2 - 4\zeta\beta_e B_{||} + \delta^2 + \Delta^2 + \zeta^2}$$

The *g*-factor is defined as the change in energy with respect to magnetic field. So, by taking the derivative of the lowest energy eigenvalue, we arrive at the analytical expression for $g_{||}$,

$$g_{||} = \frac{2}{\beta_e} \frac{dE_{1,||}}{dB_{||}}\bigg|_{B_{||}=0} = \frac{4\zeta}{\sqrt{\zeta^2+\Delta^2+\delta^2}} + 2.$$

For simplicity we have neglected orbital mixing (Δ=0). This treatment indeed reproduces the general behavior we observe in **2-NHC** where, for δ/ζ = 0.4, $g_{||}$ = 5.71 and $g_\perp \approx 0.74$, in reasonable agreement with our experimentally observed values. Despite the qualitative success of this admittedly oversimplified model, there is a subtle and surprising ramification. By examining $\hat{H}_{SOC}$, which shows that the minimum splitting of the two degenerate states is 2ζ. This implies that, to reproduce the splitting, observed in FTIR, $\zeta \leq 321.5$ cm^{-1}, which is ~54% of the free ion value (603 cm^{-1} for Ni(I)). Such a large reduction would require significant electron delocalization onto the ligands. The value would be further reduced by any deviation from complete degeneracy, where the zero-field energy separation between the two doublets becomes $2\sqrt{\delta^2 + \zeta^2}$. Such a large reduction in ζ is unphysical and inconsistent with the CASSCF results.

As mentioned in the main text we can qualitatively reproduce the observed splitting and anisotropy of the *g*–values by adding an additional orbital to the analysis. If we assume a perfectly degenerate set of pure x^2-y^2, xy, and z^2 orbitals and examine the effect of spin-orbit coupling we arrive at:

$$\hat{H}_{SOC} = \frac{\zeta}{2S}\hat{L}_z\hat{S}_z,$$

$$\begin{array}{c} \\ +2\alpha \\ -2\alpha \\ 0\alpha \\ 0\beta \\ +2\beta \\ -2\beta \end{array} \begin{array}{c} \begin{array}{cccccc} +2\alpha & -2\alpha & 0\alpha & 0\beta & +2\beta & -2\beta \end{array} \\ = \begin{bmatrix} -\zeta & 0 & 0 & 0 & 0 & 0 \\ 0 & +\zeta & 0 & 0 & 0 & 0 \\ 0 & 0 & 0 & 0 & +\zeta & 0 \\ 0 & 0 & 0 & 0 & 0 & -\zeta \end{bmatrix} \end{array}$$

Which results in three doublets each separated by ζ or ~600 cm^{-1}. This is in good agreement with the FIRMS result.

Ab initio results

Table S 3. Energies (cm^{-1}) of the spin free (non-relativistic) and SOC-corrected excited states calculated with CASSCF(9,5)/NEVPT2/def2-TZVP.

2-6Xyl		**2-7Mes**		**2-6Mes**		**2-7Xyl**	
spin free	**SOC**	**spin free**	**SOC**	**spin free**	**SOC**	**spin free**	**SOC**
254	653	64	277	189	514	79	407
302	1087	400	1101	381	1118	338	1090
3064	3430	2921	3271	2886	3357	2397	2992
3068	4009	3070	3853	3288	4042	3427	4110

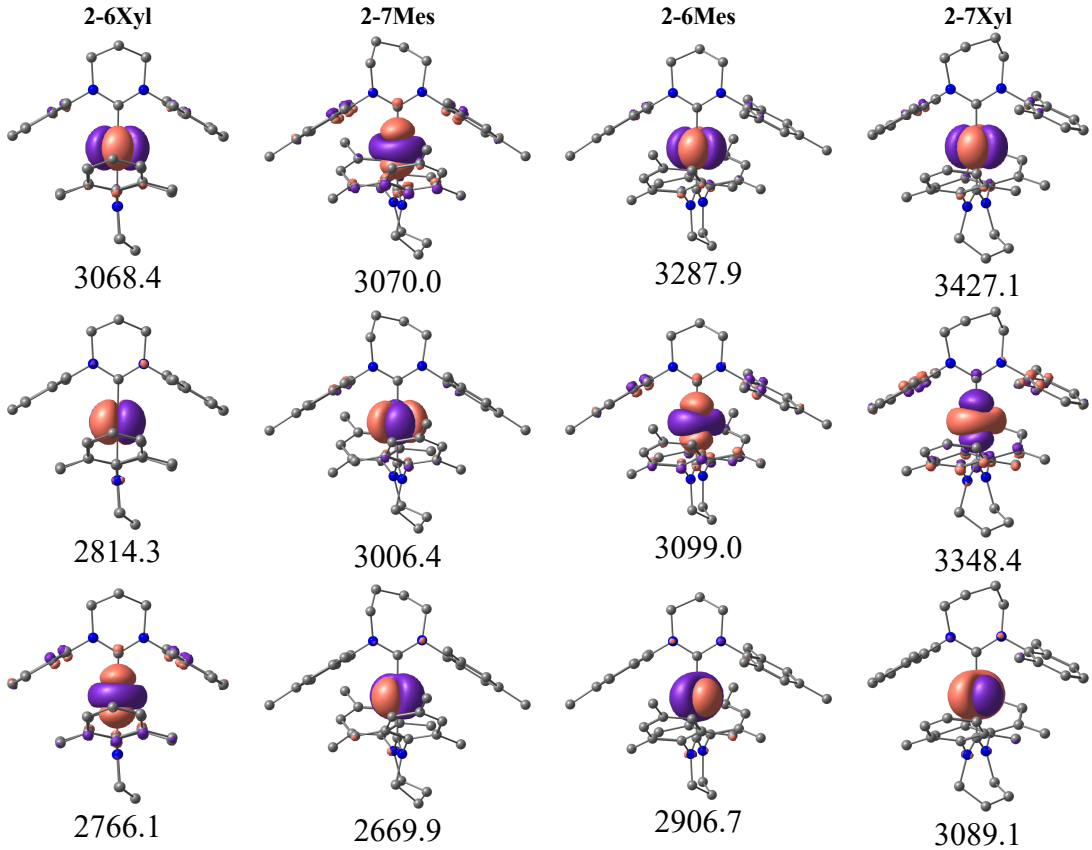

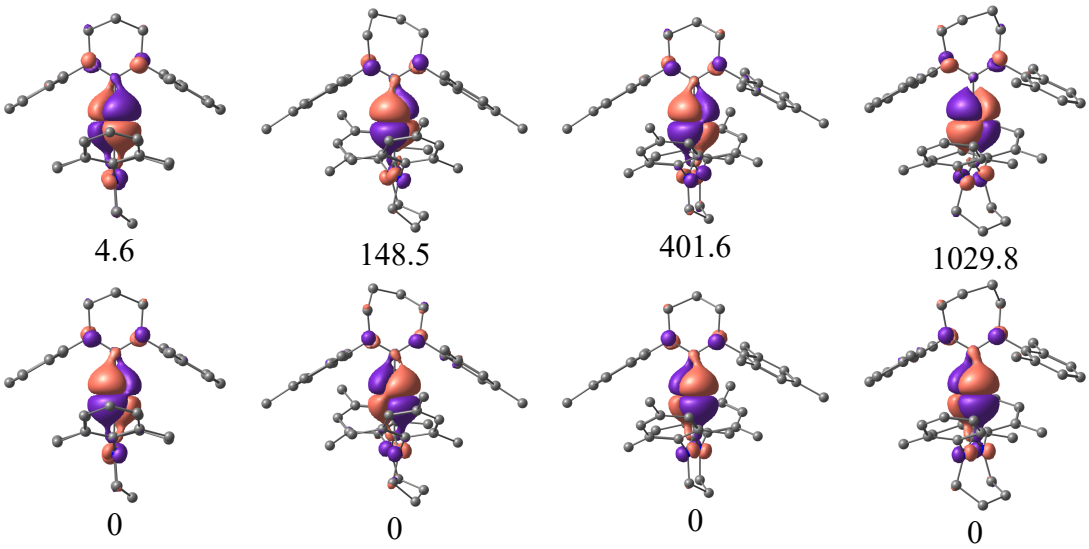

Figure S 18. AI LFT orbitals and their energies in (cm^{-1}) calculated with CASSCF(9,5)/NEVPT2/def2-TZVP.

References

1. Reta, D.; Chilton, N. F., Uncertainty estimates for magnetic relaxation times and magnetic relaxation parameters. *Phys. Chem. Chem. Phys.* **2019,** *21* (42), 23567-23575.